Gemological and Trace Element Characteristics of Cassiterite from Yunling, China

Wenqing Huang, Jungui Zhou, Ting Shui, Junyi Pan, Fanwei Meng, Rui Zuo, Shuxin Dong, and Suqiao Cao

The Yunling area in Yongde County of China's Yunnan Province is a significant source of gem-quality cassiterite. This study is an initial report on the gemological characteristics, internal features, absorption spectra, and trace element chemistry of this material.

Cut stones from Yunling typically range from 1 to 2 ct, and larger ones exceeding 20 ct are generally rare. Their colors range from near-colorless to various tones of brown, light brown, brownish pink, light gray, and black. Red color, resulting from iron oxide staining within fractures, is rare and was observed in only one of the stones we examined. The samples from this study had a specific gravity of 6.85–7.04 and did not fluoresce under long-wave or short-wave UV light. Internal features included concentric brown bands, irregular zones of gray to black colors, and multiphase fluid inclusions, with tourmaline and beryl as the primary mineral inclusions. Mica inclusions, though less frequent, were also observed.

Among the seven color groups identified for this cassiterite, chemical analyses revealed variable levels of titanium (8.08–1155 ppmw) and iron (26–425 ppmw); these were the most abundant trace elements in all color groups except black. Tungsten and uranium were only enriched in the black samples. Variations in the ultraviolet/visible/near-infrared absorption spectra for the observed color differences in the cassiterite point to possible causes. Specifically, the black coloration is associated with tungsten and oxygen vacancies, while brown and red colors are influenced by oxygen vacancies and iron oxide staining, respectively. When comparing the chemical composition profiles of cassiterite from Yunling and Viloco (Bolivia), notable differences were observed in the trace element ranges and averages. Trace element plots of Sb-Ni and Fe-Nd can be useful in distinguishing between cassiterite from the two localities.

Cassiterite (SnO_2) is a common ore mineral found in tin deposits that are spatially and genetically related to highly evolved granites (Lehmann, 2021; Ni et al., 2023). These granites originate from melts that have undergone intensive fractional crystallization (Wu et al., 2017). However, cassiterite crystals are typically opaque or small, making them unsuitable for use as gem material. In rare cases, gem-quality cassiterite has been found. One well-known example is the Viloco deposit in Bolivia (Hyršl and Petrov, 1998; Hyršl, 2002). Two lesser-known locations in China, specifically Yunling in Yongde County and Amo in Ximeng County, both situated in the Yunnan Province, also produce gem-quality cassiterite (figure 1) (Moore, 2004; Ottens, 2008, 2021; Wu, 2013; Huang and Pan, 2021; Huang et al., 2023).

Cassiterite has a structure similar to that of rutile, where each tin ion is surrounded by six oxygen ions at the corners of a regular octahedron. It exhibits uniaxial characteristics and displays exceptionally high refractive index (RI; n_ω=1.990–2.010, n_ε=2.093–2.100) and birefringence values (0.096–0.098) (Deer et al., 1992). Additionally, cassiterite has a very high specific gravity (SG) of approximately 7 and strong dispersion (0.071, roughly twice that of diamond). Its hardness is 6.5 on the Mohs scale, and twinning is common on {011} planes, resulting in the formation of the recognizable geniculate twin (also known as an "elbow" or "knee-shaped" twin). It is important to note that confusion with synthetic moissanite is possible because of that ma-

See end of article for About the Authors and Acknowledgments.
Gems & Gemology, Vol. 60, No. 2, pp. 168–193,
http://dx.doi.org/10.5741/GEMS.60.2.168

Figure 1. Left: A gem-quality cassiterite crystal, measuring 3.9 cm in length, in greisen matrix from the Yunling deposit. Photo by Yongming Shi. Right: This sterling silver ring features a Yunling cassiterite measuring 6 mm in diameter. Photo by Wenqing Huang.

terial's high birefringence (0.043) and dispersion (0.104).

The Yunling mine is situated near the village of Yunling in Yongde County in western Yunnan Province (figure 2). Cassiterite extracted from the mine was initially used for industrial purposes as the main ore mineral for tin in the early 1980s. However, it was later discovered that some of these ore pieces were of gem quality. In 2006, a mining company authorized by the local government began exploring tin ore until the mining rights expired in 2013 (Gu, 2010). Today, cassiterite specimens are occasionally extracted and collected by local villagers.

Considerable quantities of cassiterite have been mined as mineral specimens over the past three decades, and specimens on matrix rocks are highly sought after by mineral collectors (Ottens, 2008, 2021; Wu, 2013). Recently, a significant amount of faceted cassiterite, reportedly from the Yunling region, has appeared on the Chinese market, mainly in the provinces of Yunnan and Guangxi. However, the supply of gem-quality cassiterite is inconsistent, and it remains more of a collector's gemstone. These stones are commonly near-colorless and brown, though other color varieties such as black and brownish pink are occasionally encountered.

Documentation of the Yunling deposit has been limited, focusing mainly on the regional and deposit geology as well as the nature of the host granite (Nie et al., 2012; Wang et al., 2014; Xiao et al., 2022). Wu (2013) briefly documented the color categories and dimensions of rough cassiterite crystal specimens from the Yunling mine. However, the detailed gemological properties and chemical compositions that are

In Brief

- The Yunling area in Yunnan Province, China, represents a significant source of gem-quality cassiterite.
- Gemological examination reveals internal features such as concentric color bands, irregular gray to black domains, and mineral inclusions like tourmaline, beryl, and mica, along with multiphase fluid inclusions.
- Yunling cassiterite exhibits a wide variety of hues, caused either by lattice impurities or by iron oxide staining within fractures (for the red variety).
- LA-ICP-MS trace element analyses can provide insights into the substitutional mechanism of trace elements and separate Yunling cassiterite from those from Viloco, Bolivia.

Figure 2. A map showing the Yunling cassiterite occurrence. The nearby Amo deposit is also known to produce gem-quality cassiterite.

critical for identification, evaluation, and geographic origin determination remained lacking.

This article provides an overview of the geology of the Yunling cassiterite deposit and offers a detailed description of gemological properties, inclusion scenes, absorption spectra, and geochemical composition analysis by laser ablation–inductively coupled plasma–mass spectrometry (LA-ICP-MS).

GEOLOGICAL SETTING

Regional Geology. The Yunling cassiterite deposit is situated in the Changning-Menglian Belt of the Sanjiang Tethys tectonic region, which is at the southeastern margin of the Tibetan Plateau (figure 3, A and B). This region is recognized as one of China's significant tin belts. Tin deposits in the Sanjiang Tethys domain are found mainly in the Tengchong block, followed by the Baoshan block and the Changning-Menglian orogenic belt (e.g., Wang et al., 2014). The granitoids in the first two terranes span from the Early Paleozoic to the Paleogene periods (figure 3B). The Changning-Menglian Belt is delineated by the Kejie fault to the west and the Shuangjiang fault to the east (figure 3C), and it originated from the collision between the Tengchong-Baoshan block and the Simao block (Wang et al., 2014). Granitic rocks in the Changning-Menglian Belt (figure 3C) are primarily granodiorite in composition and fall into the high-potassium calc-alkaline series (Nie et al., 2012; Wang et al., 2014). Based on geochronological studies, the granitoids in this belt exhibit ages ranging from the Late Triassic to the

Figure 3. A: Tectonic framework of the Tibetan Plateau showing the location of the Sanjiang Tethys region; modified from Chen et al. (2014). B: Map showing major tectonic units of the Sanjiang Tethys in western Yunnan Province. The collision between the Tengchong-Baoshan block and Simao block gave rise to the Changning-Menglian Belt, representing the primary Paleo-Tethys Suture Zone. Modified from Deng et al. (2014). C: A closer view of the Changning-Menglian suture belt reveals the distribution of granitic rocks that primarily consist of Triassic-aged granodiorite (Nie et al., 2012). Two deposits of gem-quality cassiterite are found in the northern and southern portions of this metallogenic belt. These are located in the villages of Yunling in Yongde County and Amo in Ximeng County. Modified from Nie et al. (2012) and Wang et al. (2014).

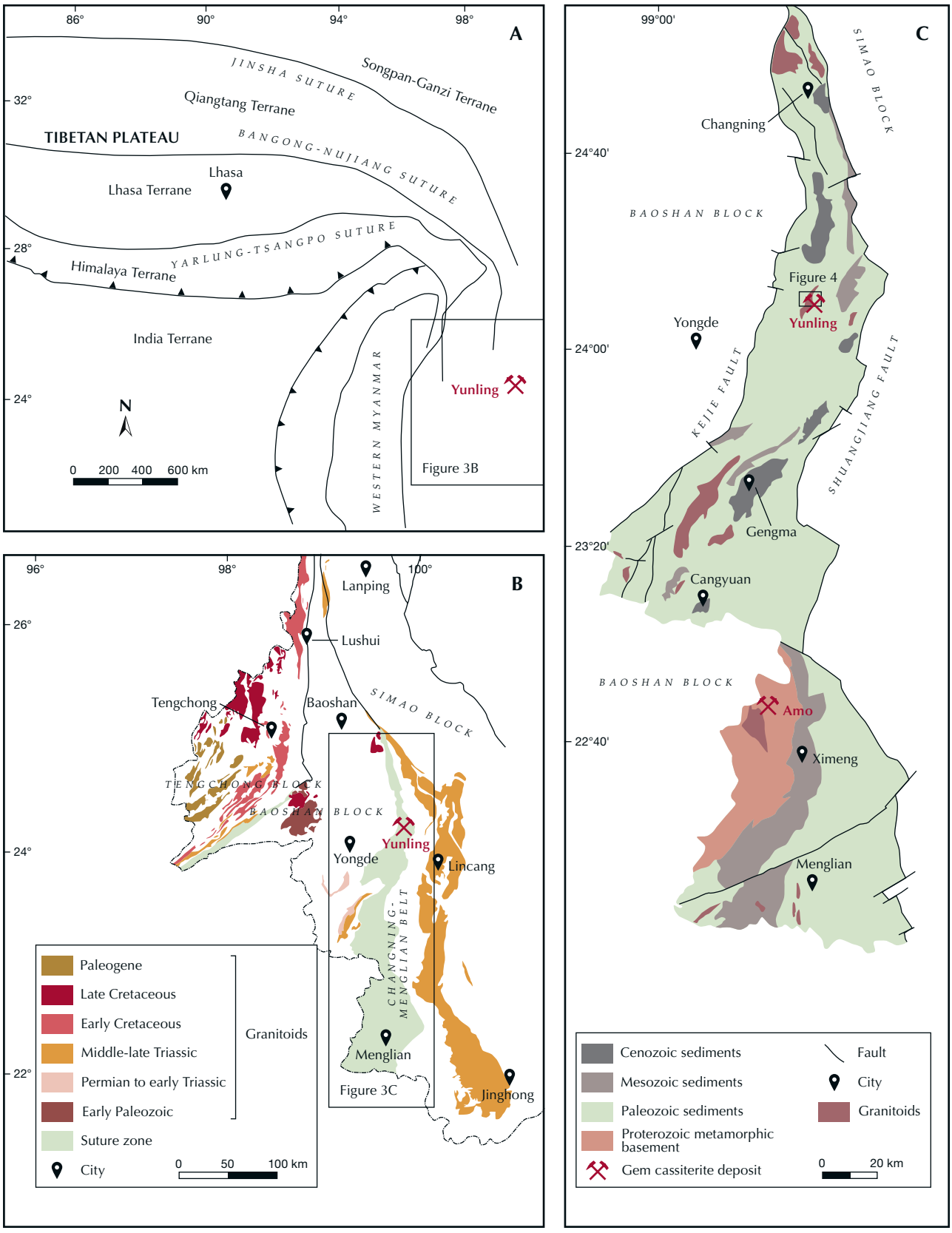
A
86°
90°
94°
98°
32°
28°
24°
JINSHA SUTURE
Songpan-Ganzi Terrane
Qiangtang Terrane
TIBETAN PLATEAU
BANGONG-NUJIANG SUTURE
Lhasa
Lhasa Terrane
YARLUNG-TSANGPO SUTURE
Himalaya Terrane
India Terrane
WESTERN MYANMAR
Yunling
Figure 3B
N
0 200 400 600 km
B
96°
98°
100°
26°
24°
22°
Lanping
Lushui
Tengchong
Baoshan
SIMAO BLOCK
TENGCHONG BLOCK
BAOSHAN BLOCK
Yunling
Yongde
Lincang
CHANGNING-MENGLIAN BELT
Menglian
Figure 3C
Jinghong
Paleogene
Late Cretaceous
Early Cretaceous
Middle-late Triassic
Permian to early Triassic
Early Paleozoic
Granitoids
Suture zone
City
0 50 100 km
C
99°00'
24°40'
24°00'
23°20'
22°40'
SIMAO BLOCK
Changning
BAOSHAN BLOCK
Figure 4
Yongde
Yunling
KEJIE FAULT
SHUANGJIANG FAULT
Gengma
Cangyuan
BAOSHAN BLOCK
Amo
Ximeng
Menglian
Cenozoic sediments
Mesozoic sediments
Paleozoic sediments
Proterozoic metamorphic basement
Gem cassiterite deposit
Fault
City
Granitoids
0 20 km

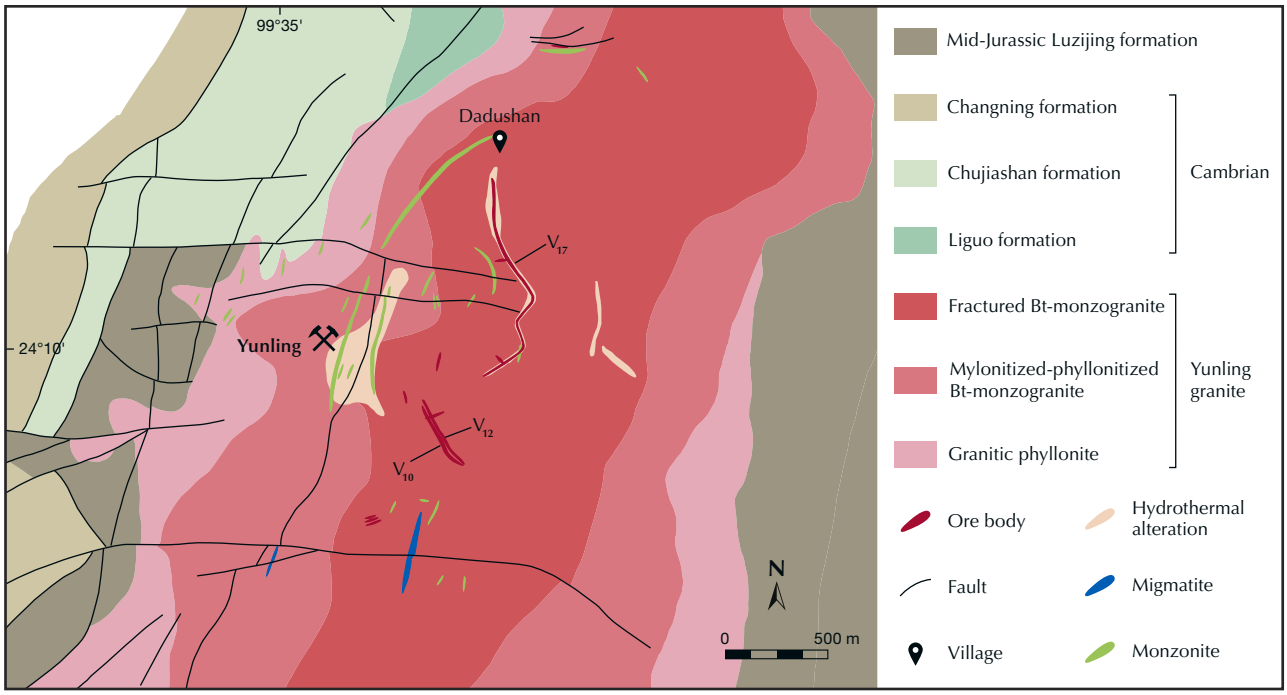

Figure 4. Geologic map of the cassiterite deposit in Yunling. Major structures in the area are EW- and NS-striking faults. The exposed plutons consist mainly of biotite monzogranite, which is of Triassic age. Additionally, there are minor occurrences of migmatite and monzonite veins. The major tin orebodies within this deposit are referred to as V_{10}, V_{12}, and V_{17}. Modified from Li (1985) and Yang et al. (1998).

Tertiary (Yu et al., 2008; Nie et al., 2012; Xiao et al., 2022). The Changning-Menglian Belt hosts several medium-sized tin deposits, including Haobadi, Yunling, and Damasa. The Amo deposit, located in the southern part of the belt (figure 3C), is also recognized for its gem-quality cassiterite (Huang and Pan, 2021).

Geology of the Deposit. The Yunling tin deposit is located in the northern section of the Changning-Menglian Belt, as shown in figure 3C. The stratigraphic sequence in this area is characterized by the Mid-Jurassic Luzijing formation, the Changning formation, the Chujiashan formation, and the Liguo formation, the latter three dating back to the Cambrian (figure 4). The intrusive rocks exposed in the region mainly consist of biotite monzogranite, referred to as Yunling granite in the Yunnan Geological Survey Report (Li, 1985), alongside minor occurrences of migmatite and monzonite veins (figure 4). The predominant rock type within the Yunling pluton is biotite monzogranite, classified as peraluminous S-type granite and belonging to the high-potassium calc-alkaline series (Nie et al., 2012; Zhang et al., 2012). Through zircon U-Pb dating, the age of the biotite monzogranite has been determined to be 231.4 ± 3.8 Ma (Nie et al., 2012).

Structurally, the major faults in the Yunling area strike in the east-west (EW) and north-south (NS) directions, with mineralization occurring mostly within the biotite monzogranite (figure 4). The primary tin orebodies, including V_{10}, V_{12}, and V_{17}, exhibit an average tin grade of 1.5%; orebody V_{17} is the largest, boasting a strike length of approximately 1000 m. Wall-rock alteration consists of greisenization, tourmalinization, and to a lesser extent, fluoritization. Ore types include cassiterite-mica-quartz-pyrite veins (figure 5) and greisen-type mineralization where cassiterite is distributed within greisenized granite. Cassiterite grains within the veins typically range from 0.1 to 1.0 mm in size, with some crystals reaching 10–20 mm or larger, characterized by high transparency and gem quality. Gem-quality cassiterite has also been reported from miarolitic cavities.

MATERIALS AND METHODS

Samples. Forty-one samples, reportedly from the Yunling area, were utilized for this study. They were acquired by author WH from Yongming Shi, a reputable collector and merchant in Yunnan Province.

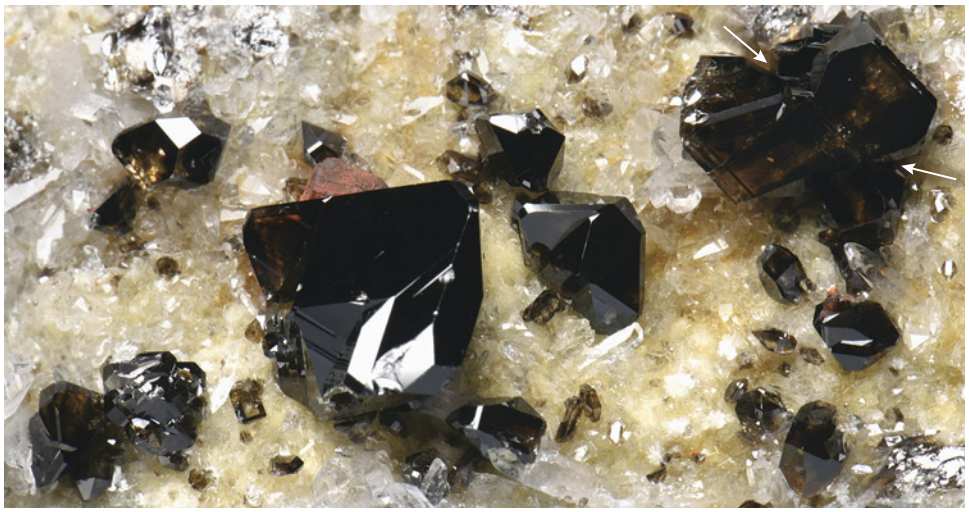

Figure 5. A cluster of transparent cassiterite crystals on the wall of a fissure vein in greisenized granite from Yunling. The presence of geniculate twins can be clearly observed at the twin interfaces, indicated by arrows. The mineral assemblage within the fissure veins consists of mica plates, cassiterite, and quartz. Some pyrite crystals with signs of ferritization are also found, though they are relatively minor. Photo by Junyi Pan; field of view 4.6 cm.

The cassiterite materials were sourced from orebody V_{17} and adjacent small-scale veins, located around 500–800 m east-southeast and 600–1100 m northeast of the Yunling village by local villagers hired by Yongming Shi. These samples comprised 17 faceted stones ranging from 0.54–2.14 ct (figure 6) and 24 rough stones weighing 10–38 ct (figure 7). Out of the 24 rough stones, 10 pieces (samples C-G1 to C-G10) underwent gemological characterization along with the 17 faceted stones, while all 24 rough stones were subsequently cut and polished into thin sections. The faceted samples were categorized into seven

Figure 6. The 17 faceted cassiterite samples from the Yunling mine (0.54–2.14 ct) examined in this study. They represent the seven color groups of cassiterite from this deposit. Photos by Wenqing Huang.

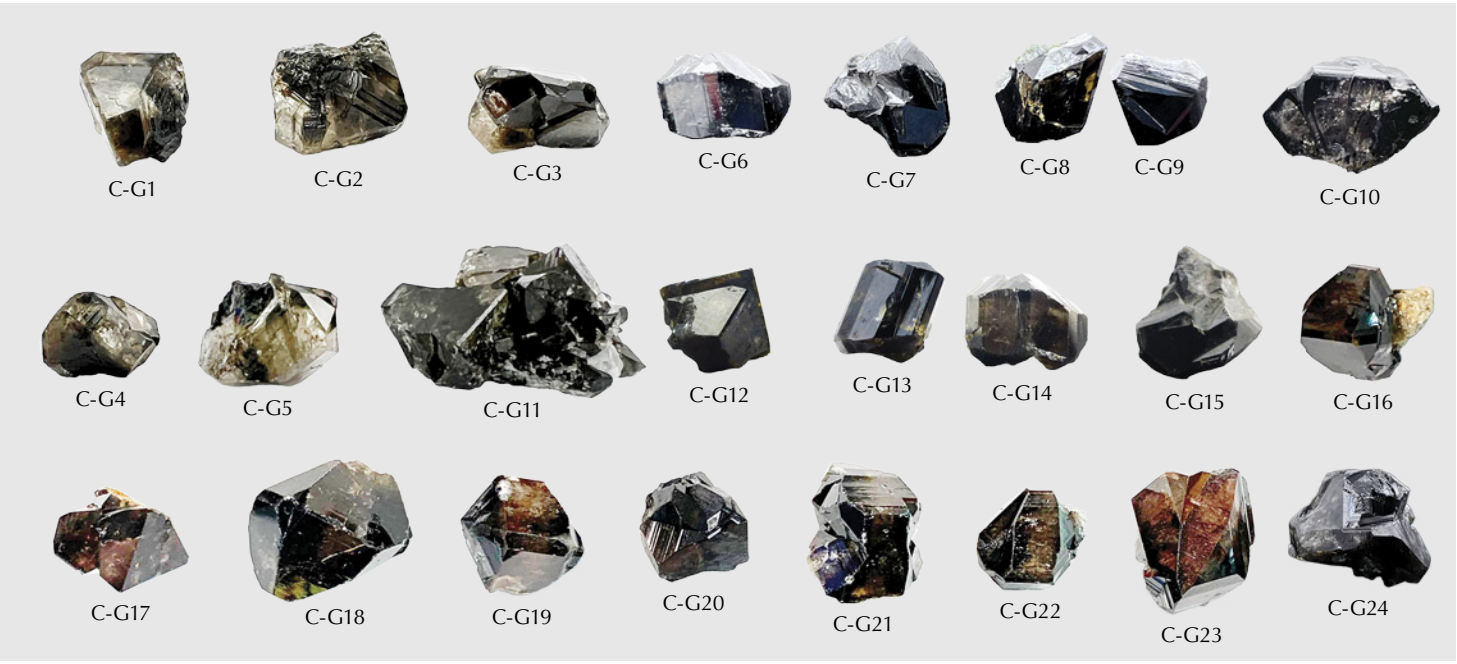

Figure 7. Rough cassiterite from Yunling. These samples typically exhibit euhedral morphologies and range from 10 ct to 38 ct. Photos by Wenqing Huang.

groups based on their color: near-colorless (two samples), light gray (two samples), light brown (five samples), brownish pink (three samples), red (one sample), brown (two samples), and black (two samples). These encompassed the full spectrum of cassiterite colors from the Yunling mine. The rough samples were cut into thin sections in specific orientations to preserve any color bands or domains and then double-side polished to a thickness of approximately 200 μm, primarily for microscopic observation and Raman spectroscopic analysis.

Standard Gemological Testing. Standard gemological analyses were completed on all 17 faceted stones and 10 of the 24 rough stones (samples C-G1 to C-G10) at the National Center of Inspection and Testing on Quality of Gold and Silver Products (NGSTC). RI was determined using an optical gem refractometer, and fluorescence reaction was determined using long-wave (365 nm) and short-wave (254 nm) UV lamps. Pleochroism was identified with a pocket dichroscope, and SG was measured through the hydrostatic method.

Microscopic Analysis and Spectroscopy. Microscopic features of the 24 cassiterite thin sections were observed using a Leica microscope attached to a digital camera, and photomicrographs were taken at magnifications ranging from 25× to 500×. To process the inclusion scenes, we employed the focus stacking technique, also known as extended depth of focus, as described by Renfro (2015). This method involves capturing a series of images at various focal planes and digitally combining them to create a single image with an extended depth of field, revealing intricate details of the inclusion scenes at different depths. For improved color distribution observation, the 17 faceted stones were immersed in methylene iodide. A gemological microscope MV5000 with diffused lighting, transmission light illumination, and a magnification of 20×–40× was utilized for observation.

To identify mineral inclusions and the compositions of fluid inclusions in cassiterite, spot analysis using Raman spectroscopy was applied on the 24 thin sections. Raman analysis was performed at the State Key Laboratory for Mineral Deposits Research, Nanjing University, using a Renishaw RM200 Raman system. An Ar^{+} laser with a surface power of 5 mW and a wavelength of 514.5 nm was used. The scanning range was set from 4000 to 100 cm^{-1}, with a grating of 1800 grooves/mm selected. Each measurement involved a 30-second accumulation time. Raman mapping was applied to measure a multi-solid inclusion using a Renishaw inVia Raman spectrometer at the Anhui Provincial Institute of Geological Experiments. The instrumental setup consisted of a 532 nm laser, a grating of 600

grooves/mm, and a spectral range of 4000–100 cm^{-1}. The mapping was conducted with a step size of 1 × 1 µm, a measurement time of 1 second per spot, and two measurements per spot. The spectrometers were calibrated daily using monocrystalline silicon at 520.7 cm^{-1}. The RRUFF database (Lafuente et al., 2016) and published literature by Wang et al. (2015) and Lensing-Burgdorf et al. (2017) were used as references for mineral phase identification.

Ultraviolet/visible/near-infrared (UV-Vis-NIR) absorption spectra were obtained on the 17 faceted stones using a BiaoQi Optoelectronics GEM-3000 spectrometer. The spectra were acquired at room temperature with a resolution of 1 nm, an integration time of 100 ms, an average of 15 measurements, a smoothing width of 1, and a scanning range of 220–1000 nm.

Trace Element Analysis. LA-ICP-MS trace element analyses were also conducted at the State Key Laboratory for Mineral Deposits Research, Nanjing University, using a Coherent 193 nm excimer laser ablation system coupled to a PerkinElmer NexION 350 ICP mass spectrometer. Both the sample and NIST 610 were loaded simultaneously into the ablation cell of a GeoLas HD system. The ICP-MS system was fine-tuned to achieve maximum sensitivity and reduce oxide production rate by maintaining ThO/Th ratios below 0.5%. The laser beam diameter was set at 32 µm with an energy density of 5 J/cm^2 and a repetition rate of 10 Hz. NIST 610 glass was applied as the bracketing external standard. A wide array of isotopes were analyzed, including ^{7}Li, ^{9}Be, ^{23}Na, ^{24}Mg, ^{27}Al, ^{29}Si, ^{39}K, ^{44}Ca, ^{45}Sc, ^{49}Ti, ^{51}V, ^{52}Cr, ^{55}Mn, ^{57}Fe, ^{59}Co, ^{60}Ni, ^{65}Cu, ^{66}Zn, ^{69}Ga, ^{72}Ge, ^{75}As, ^{85}Rb, ^{88}Sr, ^{89}Y, ^{90}Zr, ^{93}Nb, ^{95}Mo, ^{107}Ag, ^{111}Cd, ^{115}In, ^{121}Sb, ^{133}Cs, ^{137}Ba, ^{139}La, ^{140}Ce, ^{141}Pr, ^{146}Nd, ^{147}Sm, ^{151}Eu, ^{157}Gd, ^{159}Tb, ^{163}Dy, ^{165}Ho, ^{167}Er, ^{169}Tm, ^{173}Yb, ^{175}Lu, ^{178}Hf, ^{181}Ta, ^{182}W, ^{208}Pb, ^{209}Bi, ^{232}Th, and ^{238}U. Each spot measurement incorporated 20 s instrumental background, 20–30 s sample ablation, and 20 s washout time. Five to six spots devoid of inclusions were chosen for each sample ablation. A total of 91 analyses were conducted on the 17 faceted samples, using SILLS software for data reduction and tin as the internal standard (Guillong et al., 2008).

RESULTS

Gemological Properties. The gemological features of the 17 faceted samples and 10 rough stones (samples C-G1 to C-G10) show a range of hues, including brown, red, gray, and black. All were transparent, with RI values exceeding 1.78. SG values varied between 6.85 and 7.04, and this variability was broadly associated with the abundance of fractures and inclusions. Moreover, all samples showed an inert response to both long- and short-wave UV radiation. While most samples displayed no pleochroism, the brownish pink specimens exhibited moderate pleochroism of light brownish pink in one direction and pink in another. It is crucial to note that due to the rarity of cassiterite in gemological labs (Crowningshield, 1960; Gaievskyi and Iemelianov, 2012), its thermal conductivity (comparable to diamond's) along with its electricity conductivity and birefringence could lead to the misidentification of faceted colorless stones as moissanite (Hyršl, 2002).

Microscopic Characteristics. Examination with a gemological polarizer revealed that some of the thin sections of cassiterite crystals exhibited twinning, which was also present in a few of the faceted stones. Irregularities in color, such as bands and domains, were relatively common in the Yunling cassiterite

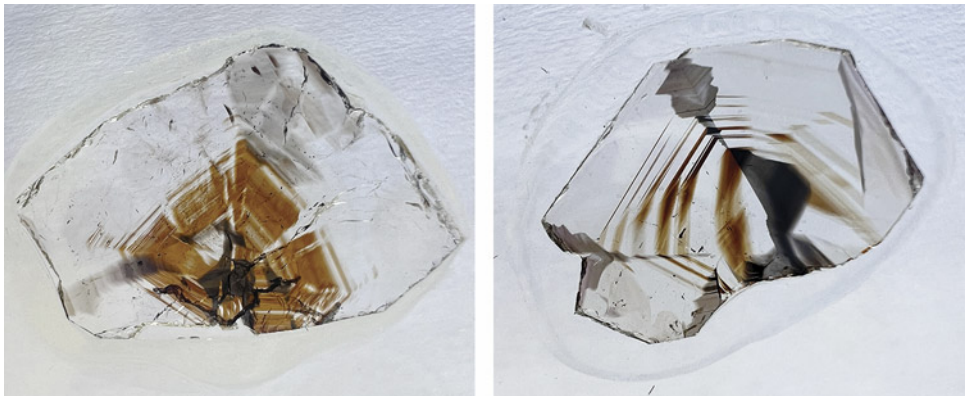

Figure 8. Alternating brown color bands and gray-black domains are relatively common in Yunling cassiterite, as shown in these two thin sections, measuring 1.81 × 1.21 cm (left) and 1.62 × 1.16 cm (right). Photos by Wenqing Huang.

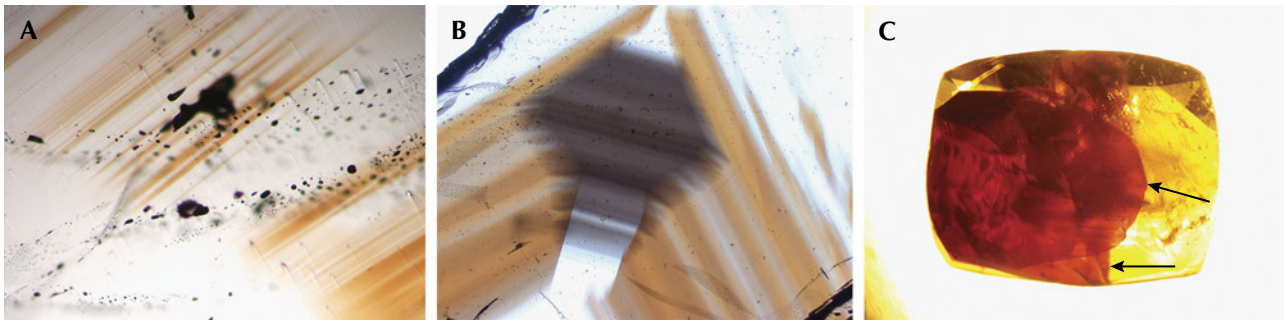

Figure 9. Color heterogeneity of cassiterite from Yunling. A: Fine brownish yellow color bands. B: Gray color domain. C: The red color observed in the red sample, viewed in immersion, appears to be confined to two fractures and distributed within planes (indicated by arrows). This distribution suggests that the red color is caused by iron oxide staining within the fractures. Photomicrographs by Wenqing Huang; fields of view 1.2 mm (A), 3.9 mm (B), and 10 mm (C).

(figures 8 and 9). The samples consistently displayed alternating color bands, typically appearing brown, while the color domains were gray to black with irregular to regular outlines (figures 8 and 9B). The red sample exhibited dark stripes, with the red color distributed exclusively along two fractures (figure 9C). Under strong fiber-optic illumination, the black samples exhibited a deep brown or deep yellowish gray color.

Microscopic observation, in combination with Raman spectroscopic analysis, revealed various mineral inclusions. The most prevalent inclusions were elongated and well-formed crystals (figure 10), identified as tourmaline by Raman spectroscopy (figure 11). The Raman bands of these tourmaline inclusions closely matched those of sodium-deficient schorl (Lensing-Burgdorf et al., 2017). These tourmaline inclusions were found as isolated occurrences (figure 10A) as well as clusters (figure 10, B–D). Further microscopic observation unveiled longitudinal striations on the column surface of these tourmaline crystals (figure 10, A and B), a characteristic feature of tourmaline.

Some mineral inclusions observed in these samples were positively identified by Raman as beryl (figures 12 and 13). The beryl inclusions presented two distinct appearances: one platy (figure 12, left) and the other prismatic (figure 12, right).

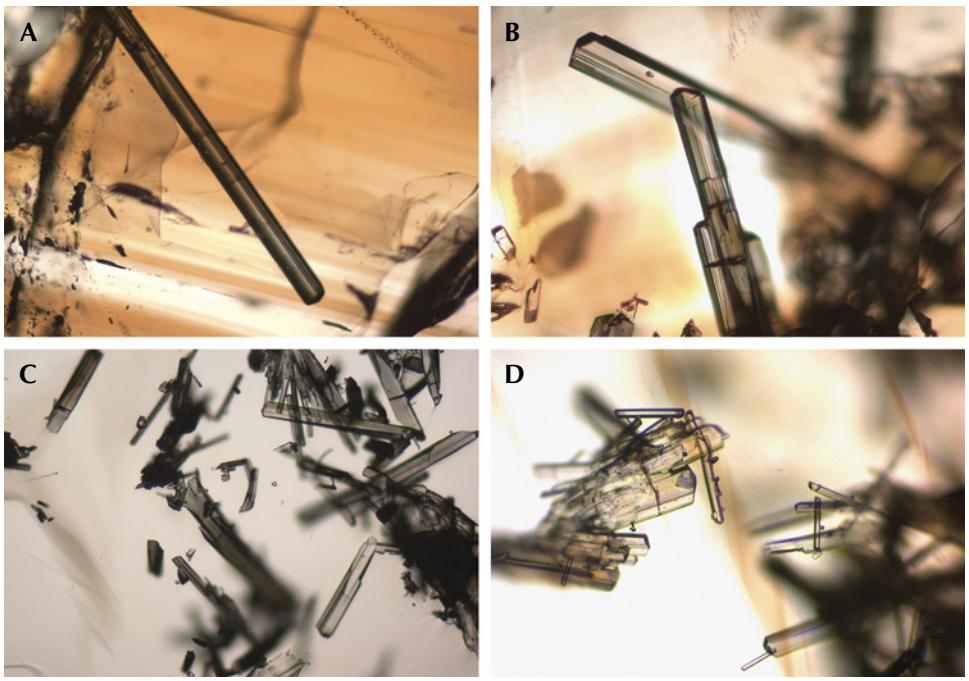

Figure 10. Internal features of Yunling cassiterite: an elongated tourmaline crystal in sample C-G8 (A) and clusters of tourmaline inclusions in samples C-G17 (B) and C-G16 (C and D). Photomicrographs by Wenqing Huang; fields of view 1.23 mm (A–C) and 0.6 mm (D).

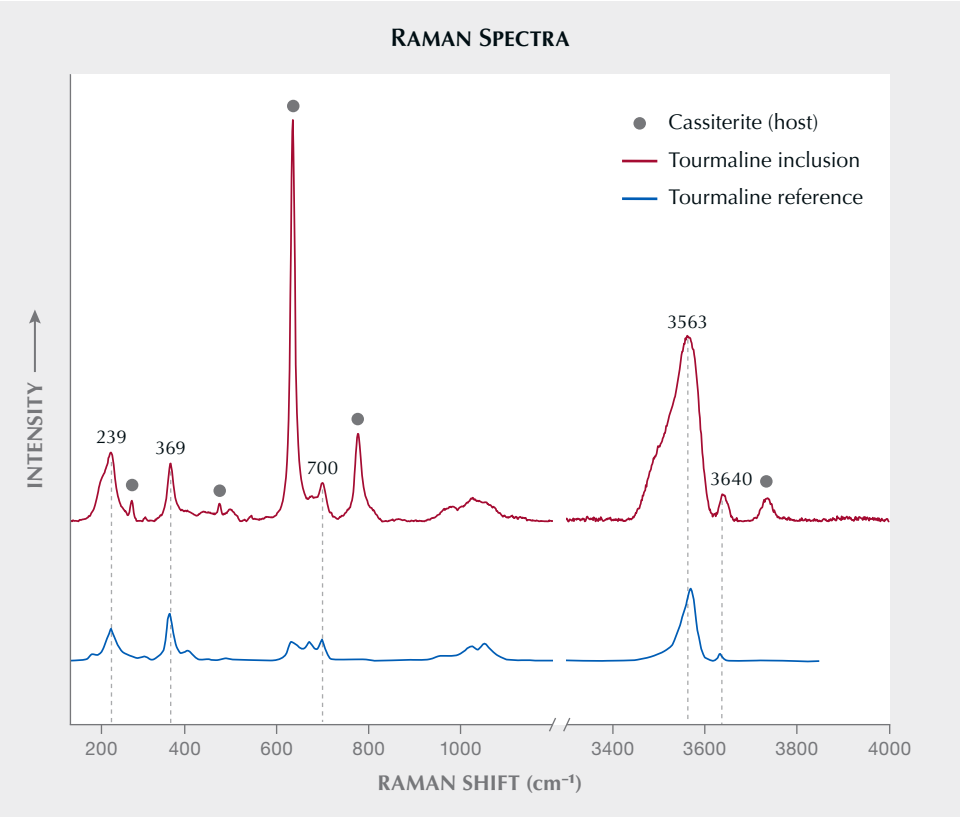

Figure 11. Baseline-corrected Raman spectra of a tourmaline inclusion in Yunling cassiterite sample C-G16 compared with the reference spectrum for tourmaline (sodium-deficient schorl) provided by Lensing-Burgdorf et al. (2017). Bands denoted by gray circles correspond to vibrations originating from the cassiterite host.

In addition, the Raman spectra of several solid inclusions such as the one shown in figure 14 matched the reference spectrum for muscovite (Wang et al., 2015) (figure 15), confirming their identification as mica. Differentiating between subgroups based on Raman spectra was challenging, as certain subgroups, such as muscovite and paragonite, displayed similar vibrational modes (Wang et al., 2015).

The Yunling cassiterite often displayed healed fissures containing fluid inclusions (figure 16). Upon

Figure 12. Internal features of Yunling cassiterite. Left: In sample C-G19, beryl inclusions showing a platy morphology. Right: A beryl inclusion occurring as a prismatic crystal in sample C-G21. Photomicrographs by Wenqing Huang; field of view 0.56 mm.

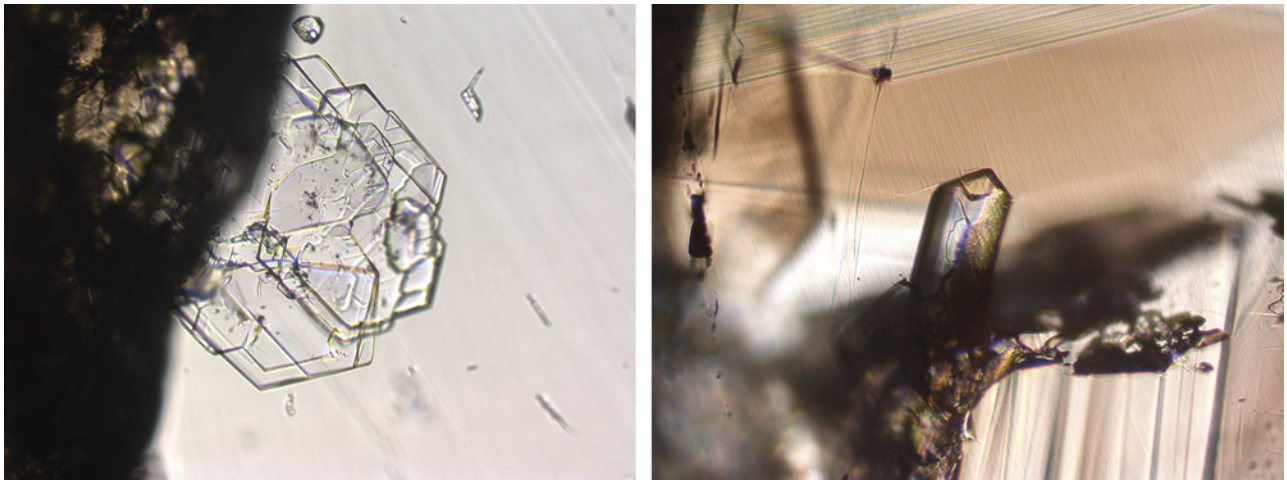

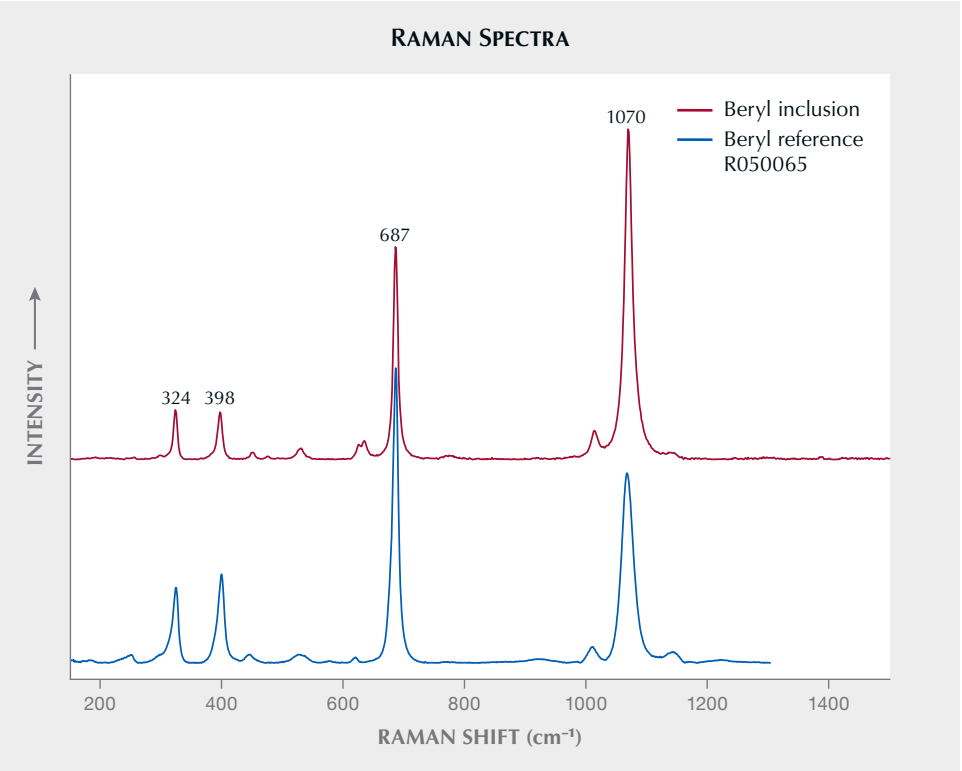

Figure 13. The baseline-corrected Raman spectrum of a beryl inclusion in sample C-G17 matches with the beryl spectrum from the RRUFF database. Spectra are offset vertically for clarity.

closer examination, these fluid inclusions consistently showed a distinct negative morphology and consisted of three phases: a bubble, a liquid, and a transparent mineral (figure 16, B, D, and E). Although the transparent mineral showed no Raman signal, this is common for halite within fluid inclusions (Frezzotti et al., 2012). The cubic morphology strongly suggests that the mineral is halite. The con-

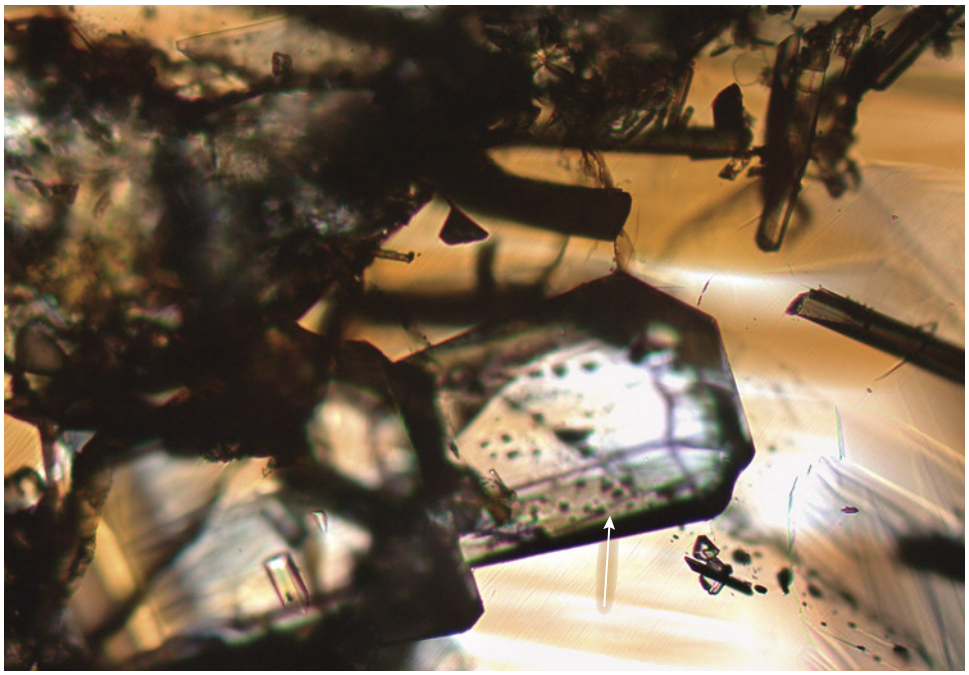

Figure 14. A mica inclusion (indicated by the arrow) in Yunling cassiterite sample C-G17. Photomicrograph by Wenqing Huang; field of view 1.13 mm.

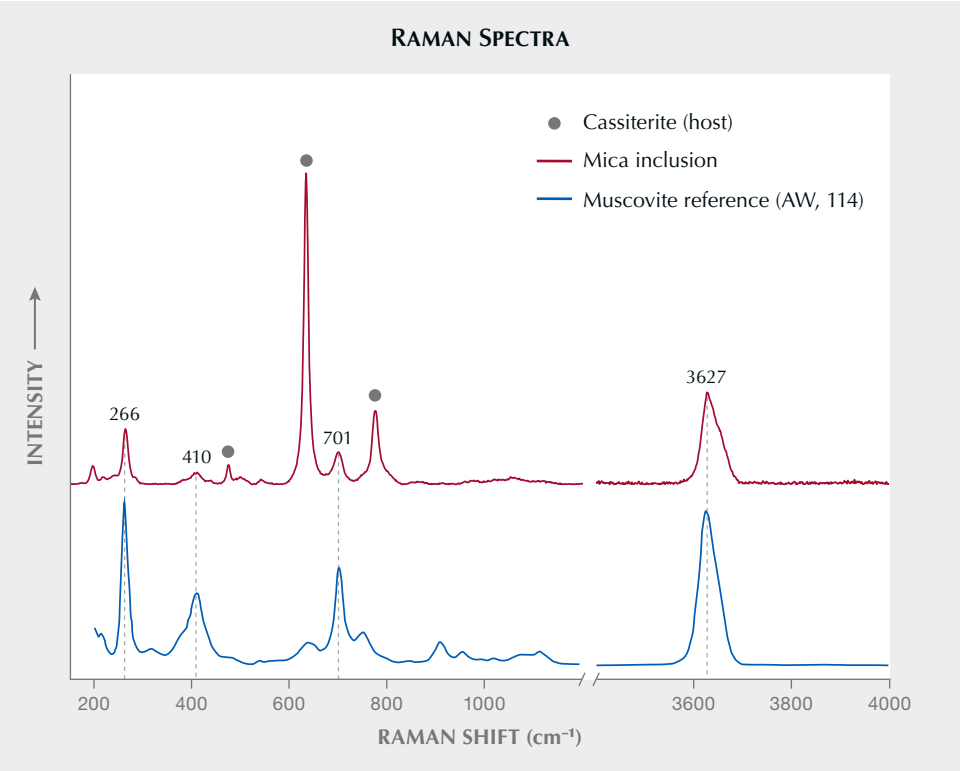

Figure 15. Raman spectrum of a mica inclusion in Yunling cassiterite sample C-G19 matched with the reference spectrum for muscovite from Wang et al. (2015). The bands marked by gray circles correspond to vibrations originating from the cassiterite host.

sistent phase ratios between the halite and the volatiles indicate that halite is a daughter mineral formed through the crystallization of the cooling fluid inclusions. Halite-bearing inclusions were the

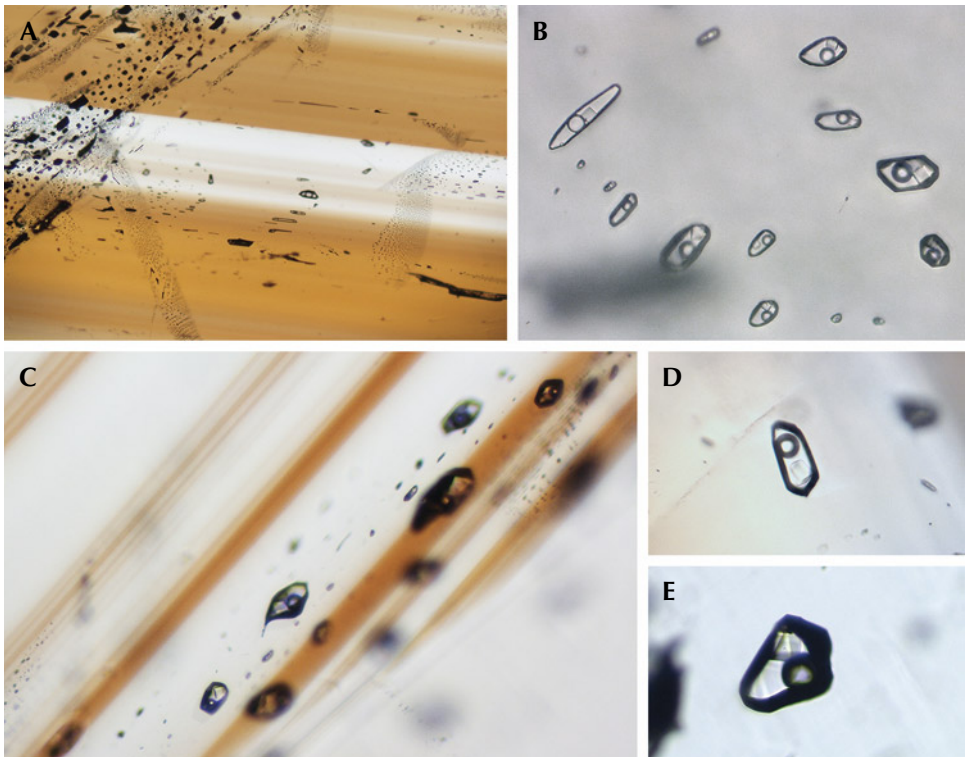

Figure 16. Fluid inclusions in cassiterite samples from Yunling. A and B: Fluid inclusions in healed fractures within samples C-G7 and C-G5, respectively. C: In sample C-G22, fluid inclusions occur parallel to the color bands. D and E: Representative three-phase inclusions in sample C-G24 show a cubic daughter mineral, a bubble, and a fluid phase. Photomicrographs by Wenqing Huang; fields of view 2.54 mm (A), 0.22 mm (B), 0.53 mm (C), 0.20 mm (D), and 0.15 mm (E). Image B was taken under transmitted light and enhanced with focus stacking techniques.

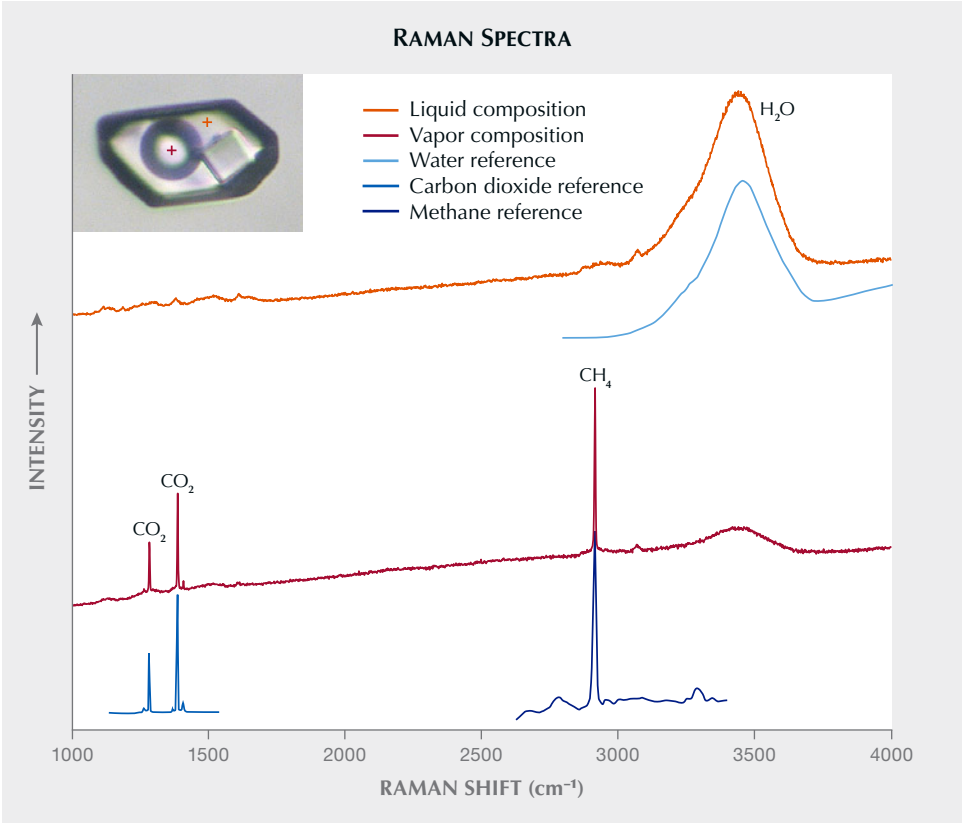

Figure 17. Representative Raman spectra showing the liquid composition and gas compositions of a fluid inclusion in Yunling cassiterite sample C-G5. These components were identified by reference to Frezzotti et al. (2012). Inset field of view 0.043 mm.

most abundant type in Yunling cassiterite. Raman spectroscopy revealed that the liquid was water, while the vapor primarily consisted of carbon dioxide and methane, identified by the characteristic bands around 1383/1282 cm^{-1} and 2916 cm^{-1}, respectively (Frezzotti et al., 2012) (figure 17).

Multiphase, multi-solid inclusions, shown in figure 18, were occasionally encountered. These oc-

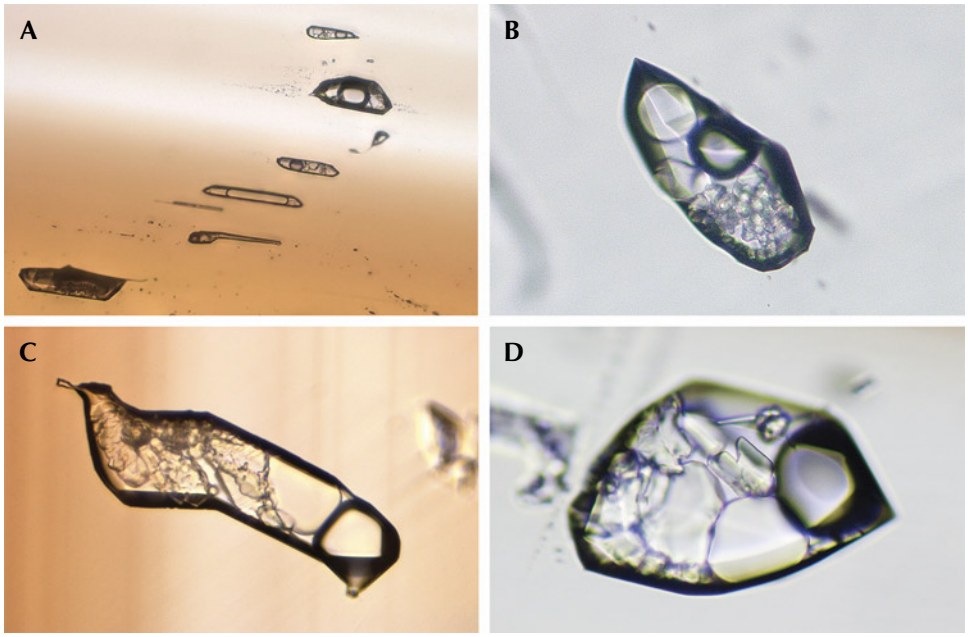

Figure 18. Multiphase, multi-solid inclusions were occasionally encountered, either in healed fractures (A, sample C-G7) or as isolated inclusions (B and D, sample C-G6; C, sample C-G8). Image A was taken using transmitted light and enhanced by focus stacking techniques. Photomicrographs by Wenqing Huang; fields of view 0.49 mm (A), 0.15 mm (B), 0.18 mm (C), and 0.14 mm (D).

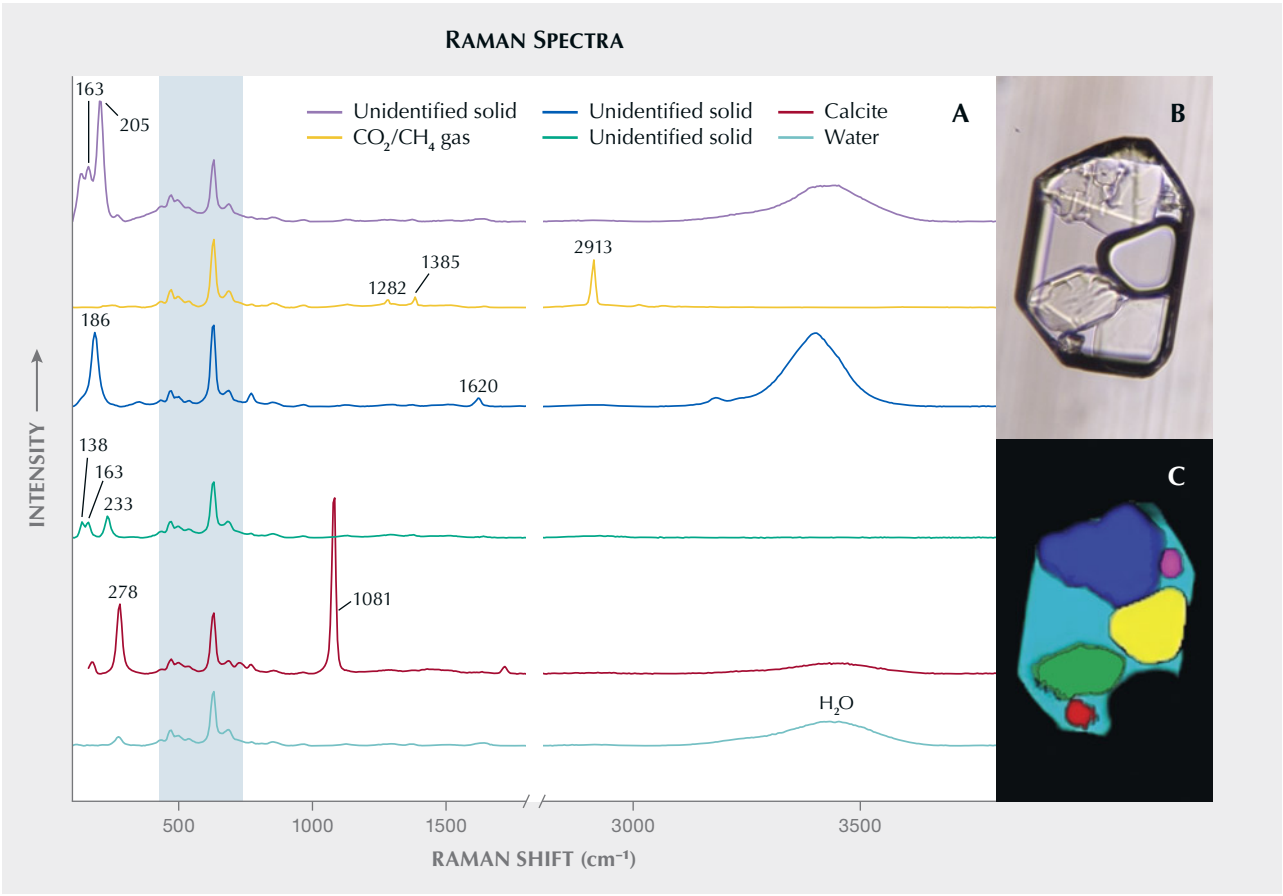

Figure 19. The Raman map (C) and corresponding baseline-corrected Raman spectra (A) of a selected multi-phase, multi-solid fluid inclusion in sample C-G8 (B; field of view 0.095 mm). The solid in the bottom right of the inclusion showed no Raman bands and is possibly halite. Three of the regions in the imaged inclusion (purple, blue, and green) could not be identified. Major Raman bands of the host cassiterite are highlighted in the light blue area of the plot.

curred either in healed fractures or as isolated inclusions. Raman analysis of a representative multi-solid inclusion indicated that the primary compositions of the liquid and vapor were water and carbon dioxide–methane, respectively (figure 19). Within this inclusion, five distinct solid phases were found. One of these solids exhibited characteristic bands at 1081 and 278 cm^{-1}, indicating a carbonate, possibly calcite. The transparent mineral located in the bottom right corner of figure 19B did not display any Raman signal, suggesting the possibility of halite. The other three solid phases showed vibrations at 163–205, 186, and 138–163–233 cm^{-1}, respectively (figure 19A), but we were unable to positively identify them based on the RRUFF database references.

Trace Element Compositions. The 17 faceted samples from Yunling were analyzed by LA-ICP-MS. Table 1 presents the representative trace elements for each sample, including their concentration ranges and corresponding averages. Other elements such as lithium, beryllium, sodium, zinc, and germanium were generally below or close to the detection limits. Notably, the high apparent values of indium were influenced by interference between ^{115}Sn and ^{115}In (Pavlova et al., 2015; Gemmrich et al., 2021). Therefore, these measurements are excluded from this report.

The titanium and iron contents ranged widely, from 8.08 to 1155 ppmw for titanium and from 25.7 to 425 ppmw for iron. The red sample had the highest iron values (see table 1). Titanium was more prevalent in black and light brown cassiterite. The concentrations of magnesium, aluminum, scandium, vanadium, chromium, antimony, cesium, and hafnium were mostly below 10 ppmw, with variations within each color group. The highest aluminum concentration, reaching 31.5 ppmw, was observed in the red sample. Among the various color

TABLE 1. Trace element concentrations[a] (in ppmw) of 17 faceted cassiterites in this study, compared with the Viloco mine, Bolivia (Gemmrich et al., 2021).

Element	Near-colorless		Light Brown					Brownish pink		
	Sample C1 (5 analyses)	Sample C2 (5 analyses)	Sample C3 (6 analyses)	Sample C4 (5 analyses)	Sample C5 (6 analyses)	Sample C6 (5 analyses)	Sample C7 (6 analyses)	Sample C8 (6 analyses)	Sample C9 (5 analyses)	Sample C10 (5 analyses)
Mg	0.03–0.10 (0.05)	bdl[b]–0.05 (0.04)	0.03–0.15 (0.08)	0.09–0.09 (0.07)	0.24–0.31 (0.28)	0.06–0.15 (0.10)	bdl–0.27 (0.16)	0.05–0.13 (0.09)	0.08–0.13 (0.09)	0.13–0.28 (0.19)
Al	11.2–14.6 (12.6)	4.75–5.26 (5.11)	5.70–6.54 (6.05)	5.37–5.88 (5.57)	4.64–5.97 (5.31)	6.87–8.94 (7.73)	2.68–9.43 (4.33)	1.47–2.03 (1.81)	4.51–6.25 (5.28)	5.87–12.2 (9.99)
Sc	2.69–3.69 (3.14)	1.04–1.30 (1.20)	0.69–1.02 (0.89)	2.07–2.47 (2.24)	3.75–4.61 (4.04)	1.80–4.23 (2.96)	1.68–6.04 (2.49)	1.14–1.75 (1.39)	1.40–1.74 (1.59)	1.15–3.89 (3.01)
Ti	162–217 (183)	77.3–114 (99.8)	138–205 (163)	193–285 (244)	989–1153 (1070)	171–566 (391)	142–723 (361)	301–390 (338)	223–318 (271)	494–875 (613)
V	2.63–4.58 (3.32)	0.97–1.22 (1.09)	1.43–2.08 (1.82)	6.74–7.68 (7.31)	14.8–19.5 (16.8)	2.98–6.27 (4.49)	6.26–9.73 (7.25)	0.70–1.47 (1.00)	1.12–1.72 (1.45)	3.19–18.8 (12.2)
Cr	1.39–2.33 (1.79)	bdl–2.51 (1.74)	bdl–2.50 (1.82)	1.53–2.70 (2.12)	7.14–9.61 (8.67)	bdl–3.28 (2.66)	1.45–2.96 (2.27)	1.20–2.42 (1.65)	bdl–3.40 (2.28)	1.83–4.27 (2.89)
Fe	173–217 (197)	78–87 (83)	77–81 (79)	108–117 (113)	94–113 (109)	123–163 (134)	61–170 (86)	48–65 (55)	93–133 (106)	106–218 (157)
Co	8.29–9.27 (8.63)	8.46–8.98 (8.75)	8.80–9.08 (8.94)	8.90–9.80 (9.23)	8.83–9.36 (9.09)	8.60–9.48 (9.11)	8.95–9.70 (9.37)	9.15–9.79 (9.41)	8.87–9.66 (9.28)	9.01–9.60 (9.25)
Ni	57.4–61.6 (59.7)	56.8–60.8 (59.4)	58.3–60.6 (59.4)	58.8–61.0 (60.2)	60.9–63.7 (62.6)	59.5–65.0 (61.4)	61.8–65.6 (63.8)	62.1–65.9 (63.7)	63.3–65.7 (64.2)	63.1–65.2 (64.2)
Ga	0.14–0.25 (0.22)	bdl–0.19 (0.14)	0.07–0.13 (0.10)	0.09–0.13 (0.11)	0.12–0.17 (0.13)	0.09–0.20 (0.16)	bdl–0.20 (0.13)	bdl–0.11 (0.09)	bdl–0.17 (0.12)	0.10–0.26 (0.18)
Zr	2.12–5.63 (4.21)	0.34–0.82 (0.60)	3.78–7.59 (5.17)	0.64–1.42 (1.19)	14.6–20.5 (16.4)	0.54–33.7 (19.6)	0.23–32.6 (6.97)	12.7–22.1 (17.4)	2.15–4.45 (3.12)	3.40–9.93 (6.18)
Nb	0.22–0.29 (0.25)	0.16–0.36 (0.24)	0.55–2.49 (1.02)	0.46–3.21 (1.87)	0.92–1.51 (1.23)	0.27–16.2 (9.30)	0.19–26.3 (6.71)	7.56–12.3 (9.68)	1.77–10.6 (6.76)	11.3–46.5 (28.1)
Sb	0.56–0.67 (0.63)	0.48–0.62 (0.55)	0.40–0.59 (0.51)	0.35–0.60 (0.51)	0.58–0.77 (0.65)	0.48–0.61 (0.54)	0.52–0.67 (0.58)	0.49–0.60 (0.55)	0.59–0.78 (0.68)	0.49–0.71 (0.59)
Cs	bdl–0.02 (0.02)	bdl–0.02 (0.02)	bdl–0.02 (0.02)	bdl–0.03 (0.02)	0.01–0.03 (0.02)	bdl–0.03 (0.02)	bdl–0.03 (0.02)	bdl–0.02 (0.02)	bdl–0.02 (0.02)	bdl–0.02 (0.01)
Ba	0.12–0.28 (0.18)	bdl–0.24 (0.17)	0.09–0.35 (0.16)	bdl–0.19 (0.15)	bdl–0.25 (0.17)	bdl–0.23 (0.19)	bdl–0.23 (0.17)	bdl–0.24 (0.19)	bdl	bdl–0.17 (0.15)
Hf	0.07–0.19 (0.14)	bdl–0.04 (0.02)	0.06–0.24 (0.13)	bdl–0.10 (0.06)	0.47–1.18 (0.76)	bdl–2.36 (2.04)	bdl–2.39 (0.66)	0.66–2.02 (1.44)	bdl–0.12 (0.06)	0.09–0.43 (0.20)
Ta	0.22–0.56 (0.33)	0.10–0.18 (0.16)	0.16–1.45 (0.45)	0.21–0.39 (0.29)	0.96–1.18 (1.08)	0.10–11.6 (5.46)	0.05–23.8 (4.46)	5.46–14.3 (7.91)	0.52–1.25 (0.76)	2.07–7.42 (4.45)
W	0.84–1.09 (0.95)	0.11–0.17 (0.14)	bdl–0.14 (0.05)	bdl–0.10 (0.07)	0.17–0.44 (0.35)	0.45–0.91 (0.65)	0.25–1.05 (0.41)	bdl–0.14 (0.10)	bdl–0.36 (0.26)	0.13–0.32 (0.22)
U	0.03–0.06 (0.04)	0.01–0.04 (0.02)	bdl–0.02 (0.02)	0.01–0.03 (0.02)	0.01–0.09 (0.05)	0.02–0.12 (0.07)	0.01–0.13 (0.04)	bdl–0.03 (0.02)	0.03–0.06 (0.04)	0.04–0.75 (0.45)

[a]*Data reported in minimum to maximum values, with averages in parentheses.*
[b]*bdl = below detection limit*

TABLE 1 (continued). Trace element concentrations[a] (in ppmw) of 17 faceted cassiterites in this study, compared with the Viloco mine, Bolivia (Gemmrich et al., 2021).

Element	Brown		Black		Red	Light gray		Yunling (China) in summary (91 analyses on 17 samples)		Viloco (Bolivia) (81 analyses on 24 samples)	
	Sample C11 (6 analyses)	Sample C12 (5 analyses)	Sample C13 (6 analyses)	Sample C14 (5 analyses)	Sample C15 (5 analyses)	Sample C16 (5 analyses)	Sample C17 (5 analyses)	Range	Detection limits	Range	Detection limits
Mg	bdl–0.19 (0.08)	bdl–0.04 (0.03)	0.07–0.33 (0.20)	0.27–0.32 (0.30)	bdl–0.03 (0.02)	bdl–0.07 (0.06)	0.05–0.13 (0.07)	bdl–0.33 (0.12)	0.005–0.07	bdl–4.63 (1.20)	0.04–4.20
Al	9.86–18.2 (14.5)	9.90–20.6 (13.7)	1.00–1.83 (1.34)	0.38–0.46 (0.43)	9.81–31.5 (21.6)	3.77–5.28 (4.61)	5.15–6.53 (5.75)	0.38–31.5 (7.27)	0.05–0.13	bdl–736 (96.0)	0.19–16.1
Sc	0.22–0.57 (0.41)	bdl–0.18 (0.12)	0.86–2.28 (1.37)	1.15–1.61 (1.42)	0.38–0.76 (0.50)	0.35–0.83 (0.52)	1.33–1.86 (1.64)	bdl–6.04 (1.74)	0.04–0.10	bdl–94.2 (9.79)	0.01–1.18
Ti	18.6–61.8 (37.5)	8.08–18.9 (13.2)	396–570 (475)	1026–1155 (1085)	22.6–52.7 (32.6)	64.1–186 (139)	208–264 (241)	8.08–1155 (343)	0.05–0.65	bdl–12172 (1156)	0.17–23.6
V	0.30–0.75 (0.52)	bdl–0.14 (0.10)	0.21–0.76 (0.46)	1.58–1.88 (1.68)	0.31–0.83 (0.51)	0.31–0.66 (0.46)	2.79–4.18 (3.28)	bdl–19.52 (3.89)	0.03–0.08	bdl–849 (70.1)	0.01–0.73
Cr	1.93–2.61 (2.28)	bdl–1.92 (1.71)	bdl–2.42 (2.08)	bdl–3.12 (1.91)	1.12–1.99 (1.55)	1.72–2.64 (2.23)	1.63–2.86 (2.32)	bdl–9.61 (2.56)	0.83–1.61	bdl–465 (19.4)	0.08–9.10
Fe	149–247 (219)	123–271 (174)	35–192 (84)	26–36 (31)	148–425 (297)	65–94 (80)	85–113 (102)	26–425 (122)	5–9	400–11200 (2623)	0.34–67.1
Co	9.23–9.61 (9.41)	8.89–9.94 (9.35)	9.25–9.58 (9.45)	9.39–9.85 (9.62)	9.48–9.77 (9.62)	9.30–9.59 (9.50)	9.08–10.1 (9.64)	8.29–10.1 (9.27)	0.004–0.05	0.54–76.7 (8.31)	0.003–0.37
Ni	62.5–66.7 (64.6)	62.2–64.1 (63.2)	63.8–66.4 (65.3)	63.5–66.4 (64.9)	63.5–66.7 (64.7)	64.6–69.3 (67.4)	63.9–67.8 (65.8)	56.8–69.3 (63.2)	0.02–0.34	3.11–416 (45.0)	0.12–19.5
Ga	bdl–0.35 (0.28)	0.19–0.55 (0.32)	bdl	bdl	0.19–0.43 (0.29)	bdl	0.09–0.21 (0.15)	bdl–0.55 (0.18)	0.03–0.10	0.42–42.5 (5.60)	0.005–0.67
Zr	1.44–3.18 (2.12)	0.60–0.86 (0.69)	29.3–43.1 (35.2)	3.58–12.7 (8.29)	0.25–2.54 (0.78)	4.46–12.6 (9.38)	2.12–3.84 (2.98)	0.23–43.1 (8.63)	0.005–0.06	bdl–350 (20.7)	0.01–1.08
Nb	0.04–0.08 (0.06)	0.07–0.17 (0.12)	224–911 (460)	180–234 (213)	0.24–1.46 (0.72)	0.40–3.16 (1.40)	0.82–1.44 (1.17)	0.04–911 (46.0)	0.004–0.04	bdl–1011 (36.1)	0.001–0.10
Sb	0.51–1.54 (0.72)	0.41–0.86 (0.57)	0.65–1.03 (0.85)	1.76–2.37 (2.05)	0.53–0.67 (0.60)	0.37–0.67 (0.49)	0.53–0.61 (0.56)	0.34–2.37 (0.68)	0.01–0.12	3.25–400 (43.3)	0.004–0.53
Cs	bdl–1.33 (0.35)	bdl–0.03 (0.02)	bdl–0.03 (0.02)	bdl–0.02 (0.01)	bdl–0.02 (0.02)	bdl–0.02 (0.02)	bdl–0.02 (0.02)	bdl–1.33 (0.04)	0.002–0.03	—	—
Ba	bdl–1.28 (0.58)	bdl–0.16 (0.13)	bdl–0.31 (0.25)	bdl–0.22 (0.20)	bdl–0.20 (0.14)	bdl–0.20 (0.15)	bdl–0.11 (0.11)	bdl–1.28 (0.19)	0.02–0.22	0.57–60.6 (7.75)	0.05–6.15
Hf	bdl–0.08 (0.06)	bdl–0.02 (0.02)	1.45–2.14 (1.73)	0.06–0.26 (0.14)	bdl–0.05 (0.04)	0.32–1.19 (0.84)	bdl–0.11 (0.09)	bdl–2.39 (0.57)	0.01–0.09	0.01–6.05 (0.30)	0.001–0.11
Ta	0.04–0.18 (0.09)	0.07–0.18 (0.10)	4.86–84.3 (35.1)	0.07–0.79 (0.41)	0.18–1.93 (0.56)	0.86–1.71 (1.25)	1.37–2.63 (1.98)	0.04–84.2 (4.10)	0.003–0.03	0.003–114 (1.78)	0.0004–0.05
W	0.34–2.19 (0.78)	0.48–0.86 (0.64)	115–327 (202)	149–176 (160)	bdl–0.11 (0.08)	0.16–0.26 (0.21)	0.27–0.52 (0.36)	bdl–327 (24.6)	0.01–0.17	0.05–33138 (2729)	0.001–0.11
U	0.01–0.05 (0.03)	0.01–0.04 (0.03)	6.48–12.1 (9.75)	14.1–17.8 (15.7)	0.02–0.11 (0.06)	bdl–0.04 (0.03)	0.02–0.05 (0.03)	bdl–17.8 (1.65)	0.004–0.02	0.01–332 (17.8)	0.0002–0.05

[a]*Data reported in minimum to maximum values, with averages in parentheses.*
[b]*bdl = below detection limit*

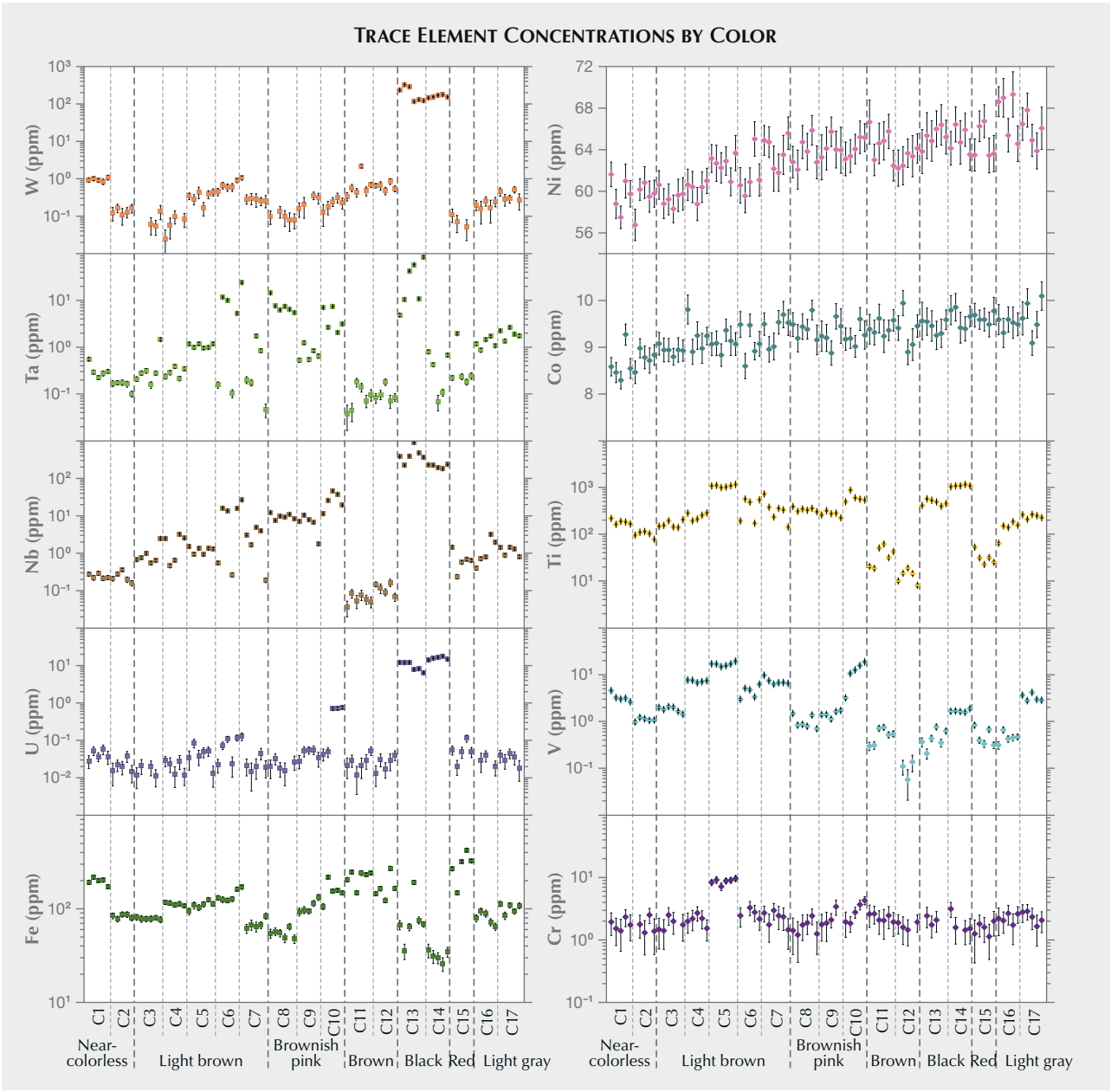

Figure 20. Selected trace element diagrams showing the geochemistry profiles of the most common chromophores in gem materials (iron, nickel, cobalt, titanium, vanadium, and chromium) and potential color-producing elements for cassiterite (tungsten, tantalum, niobium, and uranium). The individual data points represent trace element concentrations for test samples. Note that the vertical scales are different for the various elements: Nickel and cobalt are linear, while the other elements are log plots.

groups, vanadium exhibited the highest concentration in the light brown samples (19.5 ppmw) and brownish pink samples (up to 18.8 ppmw). Niobium and tungsten showed significant variation, ranging from 0.04 to 911 ppmw for niobium and from below detection limit to 327 ppmw for tungsten (table 1). The black cassiterite samples had the highest concentrations of tungsten (115–327 ppmw) and niobium (180–911 ppmw) (figure 20). The black samples also contained higher concentrations of uranium (6.48–17.8 ppmw) and zirconium (3.58–43.1 ppmw) than the other color groups (table 1). However, it is worth noting that the zirconium maximum was almost as high in the light brown (33.7 ppmw) and brownish pink (22.1 ppmw) samples. Cobalt and nickel compositions remained relatively constant across all color groups,

with ranges of 8.29–10.1 ppmw and 56.8–69.3 ppmw, respectively (figure 20).

UV-Vis-NIR Absorption Spectra. The UV-Vis-NIR spectra representative of the seven color groups are shown in figure 21 (left). A notable characteristic of near-colorless, light brown, brownish pink, and light gray cassiterite was a strong absorption band that shifted from the near-UV region (~350 nm) to the violet region (~400 nm). The brownish pink variety also showed a broad band centered around 490 nm. In contrast, the light brown and brown cassiterite exhibited increasing absorption from the red to violet regions, while the black samples displayed a relatively uniform absorption across the entire visible light range. The red cassiterite sample exhibited a broad transmission window spanning from 570 to 800 nm. Notably, the Vis-NIR reflectance spectrum of the red cassiterite closely resembled that of hematite and, to a lesser extent, goethite (figure 21, right).

DISCUSSION

Correlation Between Trace Elements and Colors. Gem materials derive their colors predominantly from dispersed metal ions, such as Cr^{3+}, Cu^{2+}, and Co^{2+}; their colors can also arise from combinations of ions, such as the intervalence charge transfer species Fe^{2+}–O–Fe^{3+} in beryl, or color centers like the GR1 center in diamond (Fritsch and Rossman, 1987, 1988a). In some cases, the presence of a colored mineral within the host can also contribute to a gem's color (Fritsch and Rossman, 1988b). However, the color-producing mechanism for cassiterite is rarely described, partly due to the scarcity of gem cassiterite with various colors.

Previous studies have attempted to establish the correlation between color variations and trace element compositions in natural cassiterite, leading to varying conclusions. Mossbauer spectroscopy has shown that cassiterite's color bears no relationship with the total iron composition but is instead influenced by the Fe^{2+}/Fe^{3+} ratios; the dark (black and brown) zones contain higher Fe^{2+}/Fe^{3+} ratios than the colorless ones (Grubb and Hannaford, 1966). On the other hand, some studies have shown that the dark zones contain higher concentrations of iron, niobium, tantalum, tungsten, and titanium (Goncharov and Filatov, 1971; Ollila, 1986; Nambaje et al., 2020). In certain cases, uranium (Swart and Moore, 1982) and uranium-tungsten (Guo et al., 2018) have been proposed as possible factors influencing the color, with higher contents corresponding to darker (dark brown) color zones. However, these interpretations are based solely on the geochemical perspective, and no optical absorption spectroscopy studies have been conducted.

Figure 21. Left: Representative UV-Vis-NIR absorption spectra for the seven colors of Yunling cassiterite. Right: Vis-NIR reflectance spectra of the red Yunling cassiterite sample, compared with those of hematite and goethite (from Harris et al., 2015).

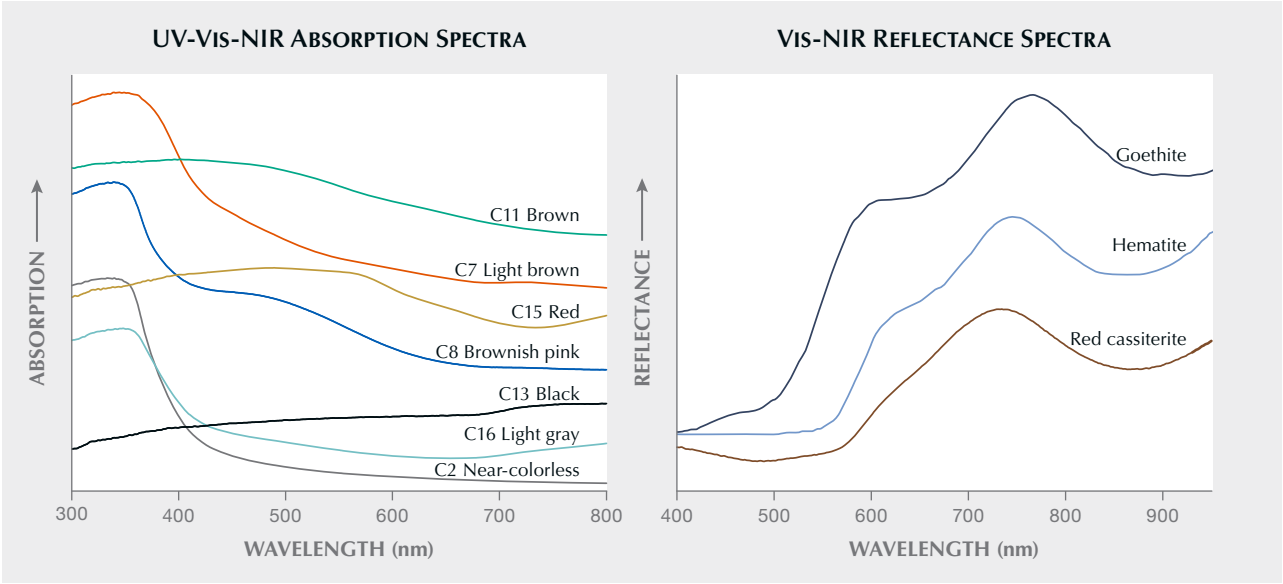

Meanwhile, the color mechanism of impurity-doped synthetic cassiterite, widely used as a pigment in the ceramics industry, has undergone extensive research. A violet color has been linked to the presence of Cr^{4+}, generating a characteristic band at 550 nm (Lopez-Navarrete et al., 2003; Serment et al., 2019). The contribution of Cr^{3+} and/or Cr^{4+} to the violet hue has also been suggested, with Cr^{3+} in cassiterite displaying characteristic bands at 650 and 470 nm (Ishida et al., 1987). Investigation by Matsushima et al. (2008) into dark brown films suggests that color origin may stem from chloride impurities and/or oxygen vacancies. Moreover, the incorporation of high field strength elements into cassiterite can alter its color appearance. For example, antimony imparts a light gray hue (Tena et al., 2005) or black (Kojima et al., 1996), attributed to charge transfer interactions between Sb^{3+} and Sb^{5+} within the matrix. These insights underscore the intricate nature of cassiterite's color mechanism, dictated by the interplay of the impurity species and their respective oxidation states.

Figure 20 shows common chromophores in gem materials (iron, nickel, cobalt, titanium, vanadium, and chromium), along with potential color-producing elements for cassiterite (tungsten, tantalum, niobium, and uranium). The consistently low cobalt and nickel concentrations across the seven color groups imply a limited role in cassiterite coloration. Notably, the iron concentrations in one near-colorless sample (sample C1) stood out from the other (sample C2; see table 1 and figure 20). Further microscopic examination of sample C1 revealed that high iron concentrations were associated with colorless areas rather than dark brown or brownish pink areas. This implies that iron does not significantly contribute to the color of pink and brown samples, as brownish pink sample C8 and light brown sample C3 were comparable in iron content to near-colorless sample C2, which had the lower iron content of the two near-colorless samples (figure 20). Although Guo et al. (2018) found higher uranium and tungsten compositions in the dark brown zones than in the light yellow domains, their low concentration in both the brown group and the light brown group suggests a minimal influence on the brown color (table 1; figure 20). In other words, impurities other than uranium-tungsten may be responsible for the brown color of Yunling cassiterite. Noticeably elevated tungsten contents are frequently found in the black cassiterite group (avg. 183 ppmw; table 1; see also Huang et al., 2023), suggesting that tungsten may contribute to the black coloration. This is supported by Zhou et al. (2018), in which doped tungsten was shown to enhance the visible light absorption of cassiterite. It is important to note that tungsten impurities in cassiterite often exist in hexavalent and tetravalent states (Möller et al., 1988; Bennett, 2021). While W^{4+} does not impact the color of cassiterite, W^{6+} can contribute to the black color through tungsten-oxygen charge transfer (Nomiya et al., 1987).

Further UV-Vis-NIR spectroscopic analysis revealed distinct absorption spectra among different colors of cassiterite (figure 21, left). Absorptions related to Cr^{3+} (650 and 470 nm) or Cr^{4+} (550 nm) were not observed in any of the samples. In brownish pink cassiterite, a broad absorption band centered at approximately 490 nm might account for its pink color; however, similar bands have not been previously reported, and the specific nature of this 490 nm band remains unclear. The absorption spectra of light brown and brown cassiterite, displaying a gradual decrease in absorption strength with wavelength, resembled the dark brown SnO_2 film presented in figure 3 of Matsushima et al. (2008). According to those authors, the dark brown coloration may stem from impurities such as chloride and/or oxygen vacancies. Oxygen vacancies are commonly found in magmatic-hydrothermal cassiterite, as reported by Grigor'yev et al. (1986), and these samples typically display a dark brown or black coloration that becomes more intense with an increased number of oxygen vacancies. Therefore, the origin of the brown (and possibly light brown) color in cassiterite from Yunling could be linked to the presence of oxygen vacancies. The color of the black cassiterite, which is influenced by tungsten, could also be associated with the presence of oxygen vacancies. The red cassiterite from Yunling exhibited a broad transmission at approximately 710 nm (figure 21, left). Microscopic examination revealed highly heterogeneous color distribution in the analyzed red cassiterite, in which the red color was concentrated exclusively in the fractures (figure 9C). Hence, iron oxide staining in the fractures, rather than trace elements or lattice defects, was likely responsible for this coloration. This inference is supported by its Vis-NIR reflectance spectrum (figure 21, right), which is highly consistent with that of hematite, a common red-colored iron oxide found in soil and sediments.

Substitutional Mechanism of Trace Elements. Cassiterite possesses a tetragonal lattice structure analogous to that of rutile, allowing the incorporation of

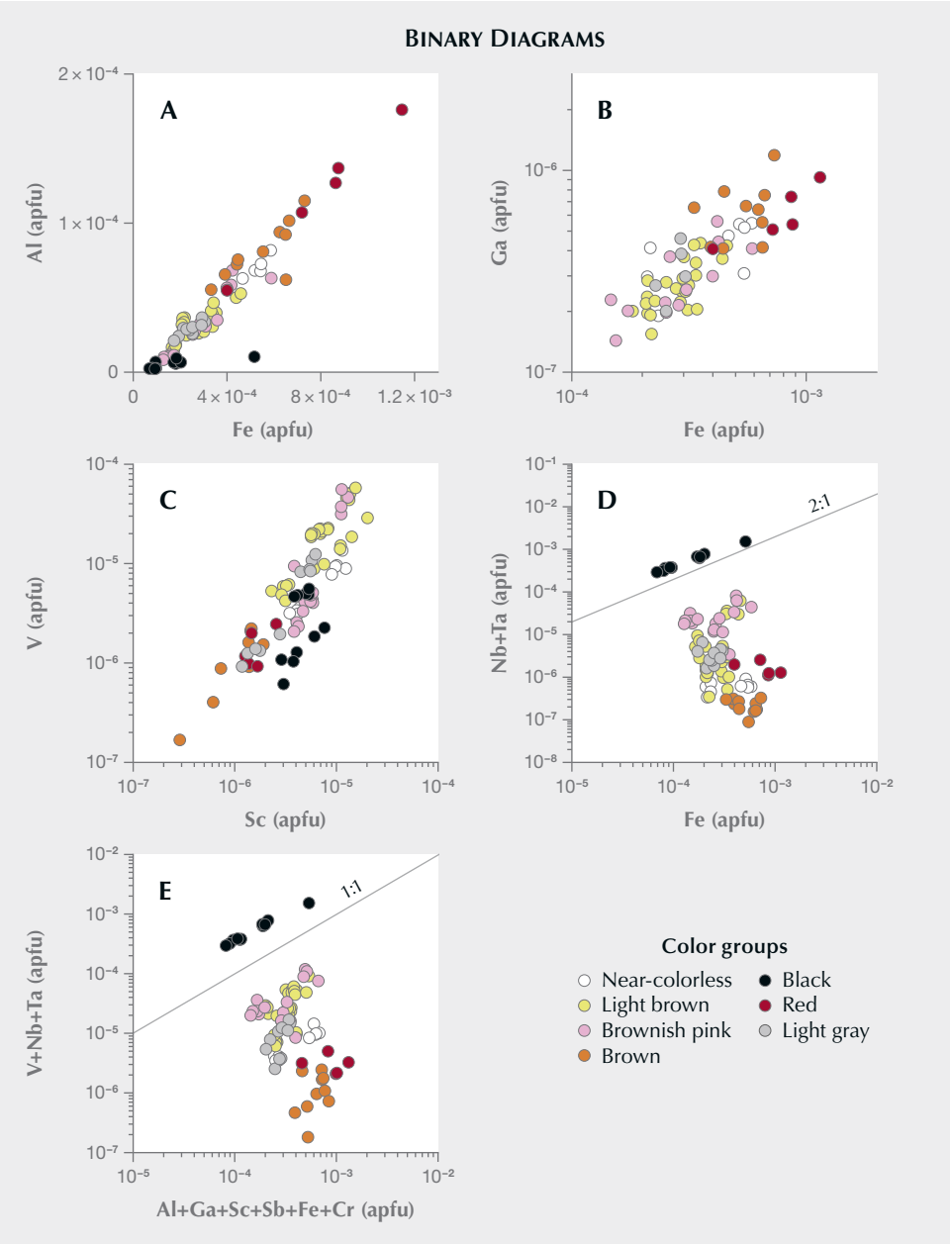

Figure 22. Binary diagrams of selected trace elements in cassiterite from Yunling, expressed in atoms per formula unit (apfu). A: The positive relationship between aluminum and iron is likely due to their similar trivalent ionic radii. B: Gallium and iron show a positive correlation, indicating a coupled substitution of $2Sn^{4+} \leftrightarrow Fe^{3+} + Ga^{5+}$. C: The positive relationship between scandium and vanadium implies that vanadium is in a valence state of +5, with a substitution mechanism of $2Sn^{4+} \leftrightarrow Sc^{3+} + V^{5+}$. D: A significant deviation from the 2:1 line in the Nb+Ta vs. Fe plot for most samples implies a significant iron excess. E: The plot comparing trivalent cations (aluminum, scandium, iron, gallium, chromium, and antimony) and pentavalent cations (vanadium, niobium, and tantalum) shows a significant excess of trivalent cations for most samples. Note that the scales are different for the various plots: A is linear, while B–E are log-log plots.

various trace elements such as iron, vanadium, scandium, titanium, tungsten, and uranium (Farmer et al., 1991; Tindle and Breaks, 1998; Bennett et al., 2020). However, the occurrence and substitution mechanisms of these trace elements are not well constrained and may vary among deposits (e.g., Gemmrich et al., 2021; He et al., 2022). The incorporation of trace elements into cassiterite depends largely on ionic charge, radius, and coordination, allowing compatibility with a wide range of elements in different valence states (e.g., Grubb and Hannaford, 1966; Möller et al., 1988; Murciego et al., 1997). Tetravalent elements such as Ti^{4+}, Zr^{4+}, and Hf^{4+} can directly substitute for Sn^{4+} without requiring additional ions for charge balance. In contrast, trivalent and pentavalent elements require other elements for charge compensation, as seen in examples such as $3Sn^{4+} \leftrightarrow 2(Ta, Nb)^{5+} + Fe^{2+}$ or $3Sn^{4+} \leftrightarrow W^{6+} + 2Fe^{3+}$.

In figure 22 we use the unit apfu (atoms per formula units) and the conversion from ppmw to apfu as follows:

$$apfu = \frac{molecular\ weight\ of\ SnO_2 \times (ppmw \times 10^{-6})}{atomic\ weight\ of\ the\ element}$$

The Fe-Al (figure 22A) and Fe-Ga (figure 22B) pairs yield a positive relationship in the Yunling cassiterite samples. This positive correlation between iron and aluminum is likely due to the similarity in trivalent ion radii (Shannon, 1976). Similarly, the Yunling cassiterite exhibited a positive correlation between iron and gallium that is analogous to what has been observed in many granite-associated hydrothermal cassiterites (e.g., He et al., 2022). This correlation can be explained by the coupled substitution of $2Sn^{4+} \leftrightarrow Fe^{3+} + Ga^{5+}$. Furthermore, the positive relationship between scandium and vanadium (figure 22C) implies that vanadium is in a valence state of +5, considering that scandium occurs only in a +3 valence state in geological conditions. Therefore, a substitution mechanism of $2Sn^{4+} \leftrightarrow Sc^{3+} + V^{5+}$ is favored.

It is well established that niobium and tantalum are incorporated into cassiterite in the pentavalent state through a coupled substitutional mechanism involving iron (Möller et al., 1988; Neiva, 1996). Figure 22D shows a marked deviation from the 2:1 line in most of the sample analyses, implying a significant iron excess. This surplus iron indicates additional substitution in the samples. Considering a broader range of trivalent (aluminum, scandium, iron, gallium, chromium, and antimony) and pentavalent (vanadium, niobium, and tantalum) cations dominant in cassiterite, the data would be expected to plot along the 1:1 ratio. However, there appears to be a deviation indicating a significant excess of trivalent cations (figure 22E). The low concentrations of lithium, mostly below detection limits, make its compensation impossible. In order to balance the uncompensated trivalent cations, potential compensating cations could be H^+ (Tindle and Breaks, 1998; Mao et al., 2020) or interstitial Sn^{2+} (as proposed by Cohen et al., 1985). Moreover, the black samples in figures 22D and 22E stand out from the other color groups on these plots. Recent studies have shown that individual cassiterite crystals exhibit distinct chemistries within each zone that appears dark in cathodoluminescence imaging, driven by specific substitution mechanisms (Bennett, 2021; Huang et al., 2023). Therefore, the observed variations observed in figures 22D and 22E could be attributed to cathodoluminescence-dark zones in the black samples (Huang et al., 2023).

Geographic Origin Determination. Although large euhedral cassiterite of gem quality from the Viloco mine in Bolivia was documented more than 20 years ago (Hyršl, 2002), comprehensive gemological properties remained lacking. Nevertheless, trace element spectra of cassiterite from the Viloco mine (Gemmrich et al., 2021) allow comparative analysis with the Yunling deposit (table 1).

Box and whisker plots in figure 23 illustrate the concentration of 12 selected elements, revealing broader ranges for elements such as tantalum, uranium, cobalt, and titanium in Viloco cassiterite compared to Yunling. Yunling cassiterite typically has a lower iron concentration, but the ranges overlap (as they do for all elements). The low iron concentration of Yunling cassiterite (generally <200 ppmw) is atypical of granite-related cassiterite deposits worldwide (Hennigh and Hutchinson, 1999; Guo et al., 2018; Chen et al., 2019). However, a granite-related petrogenesis has been suggested for this deposit (Xiao et al., 2022), supported by the vein occurrence and mineralogy comparable to other granite-related deposits. High-salinity fluid inclusions (figure 16) provide further evidence for its magmatic-hydrothermal origin. To our knowledge, the low iron content in Yunling cassiterite is unique. Iron incorporation in the cassiterite lattice typically involves other cations through a coupled substitutional mechanism (e.g., Möller et al., 1988); hence, the low iron content in Yunling cassiterite may be related to the low content of other cations such as niobium, tantalum, and gallium. Notably, the concentrations of cobalt and nickel are consistent in cassiterite from Yunling, regardless of color, while their concentrations in Viloco cassiterite are highly variable, even within a single sample (Gemmrich et al., 2021). For example, in sample Vil2-sn-b examined by Gemmrich et al. (2021), the concentrations of cobalt and nickel varied by an order of magnitude, from 8 to 77 ppm and 45 to 416 ppm, respectively. Therefore, multiple spot measurements of cobalt and nickel concentrations are valuable in separating cassiterite from Yunling and Viloco.

Figure 24 displays discrimination plots for Yunling compared to Viloco for Cr-V, U-W, Nb-Fe, and Ni-Sb. Significant overlap is observed in the Cr-V plot (figure 24A), undermining its effectiveness for discrimination. Minor overlap between uranium and tungsten points in Yunling and Viloco cassiterite is also observed in figure 24B. Comparing iron concentrations (figure 24C) and antimony concentrations (figure 24D) in Yunling cassiterite with those in Viloco cassiterite helps to distinguish their origin.

Cassiterite samples from both deposits contain healed fissures and tourmaline needles (Hyršl, 2002), but the presence of beryl and mica inclusions is typical for Yunling and Viloco.

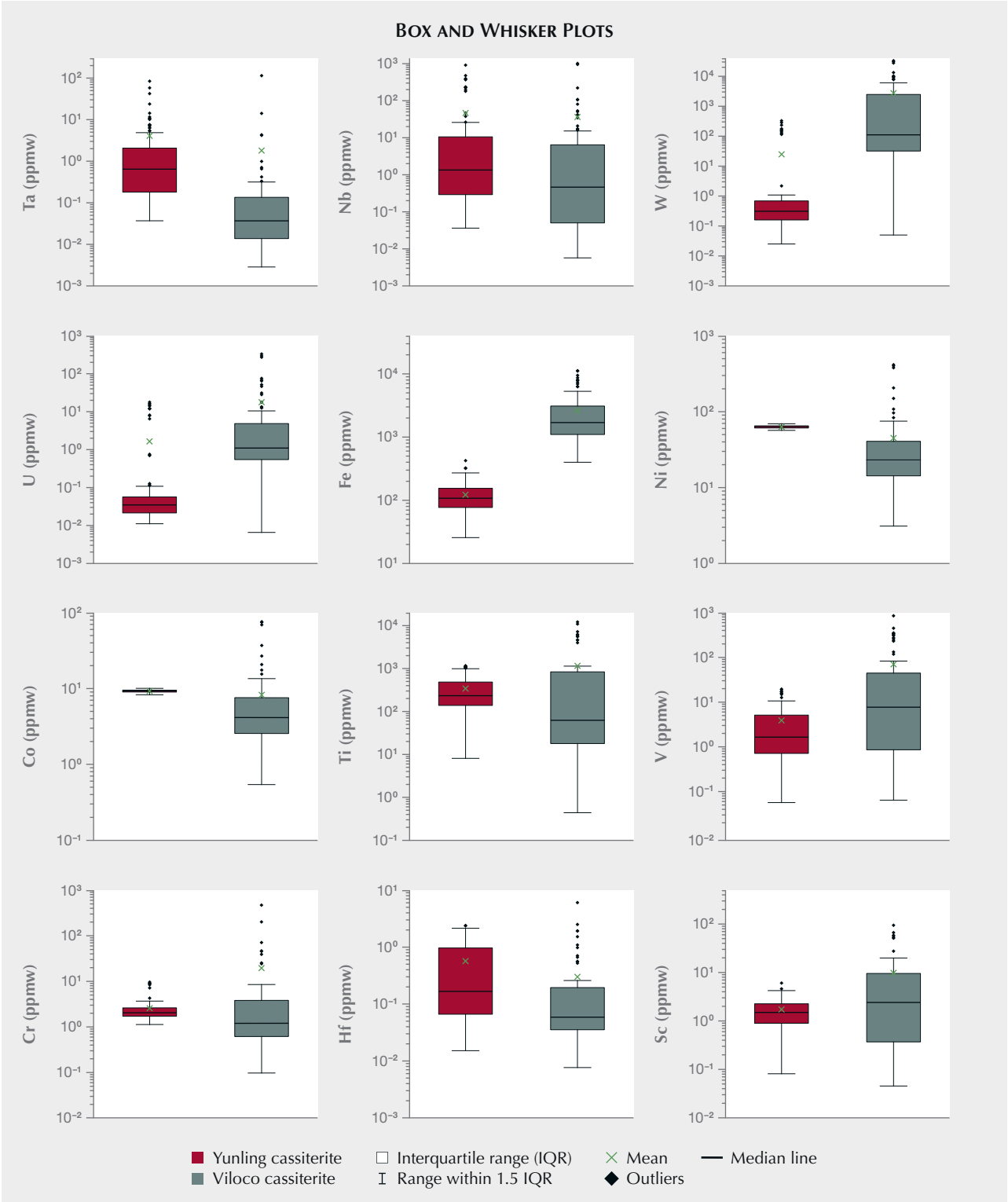

Figure 23. Selected box and whisker plots displaying trace element concentration comparisons in cassiterite from Yunling and Viloco deposits (data from Gemmrich et al., 2021). The number of analyses is 91 for Yunling and 81 for Viloco. Most elements in Viloco cassiterite (e.g., tantalum, uranium, scandium, and titanium) exhibit a wider range of spectra than those in cassiterite from Yunling. In Yunling cassiterite, the iron concentration is notably lower. Unlike Viloco cassiterite, which displays significant variations in cobalt and nickel contents, the concentrations of those elements in Yunling cassiterite remain rather consistent.

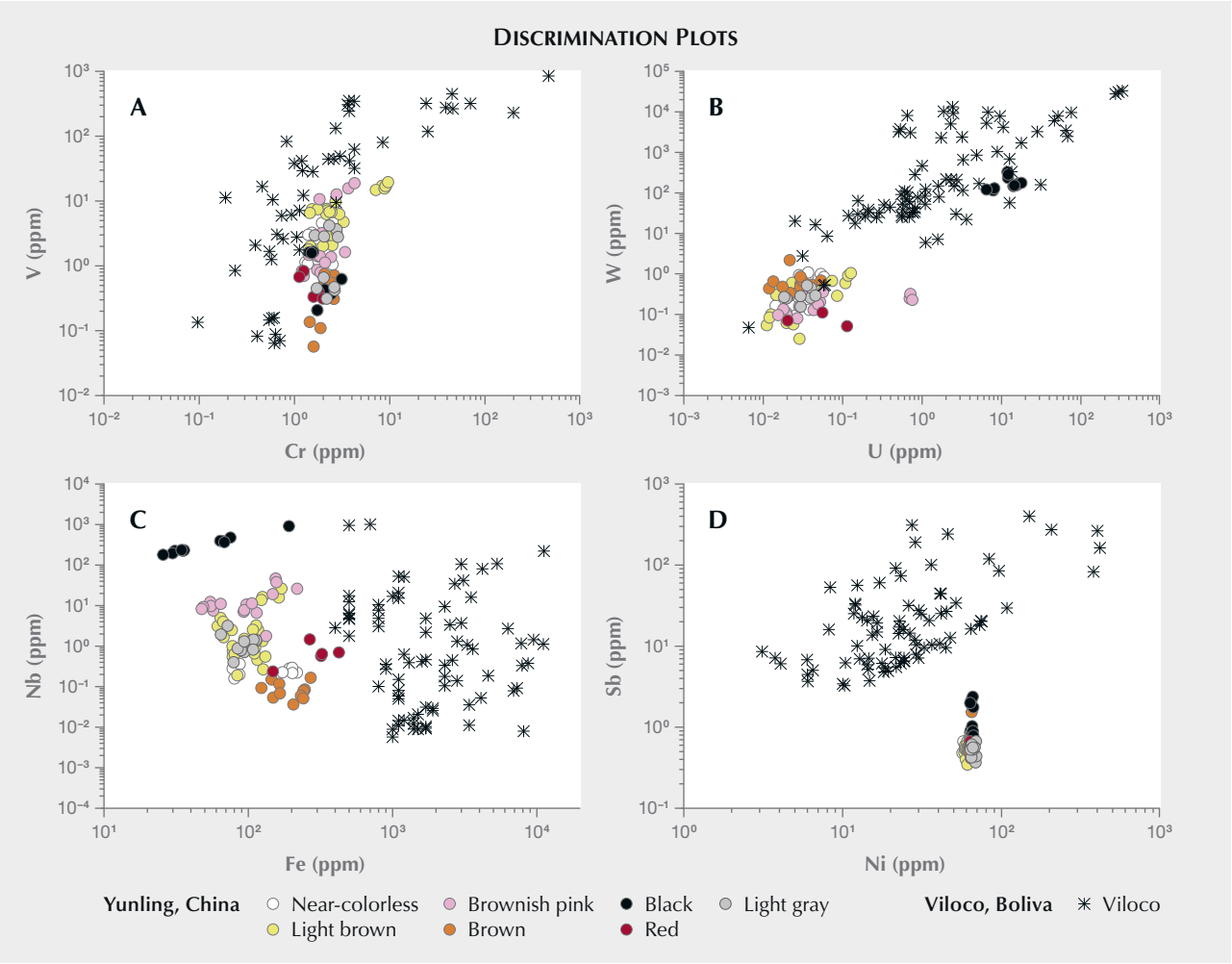

Figure 24. A: Plot of V vs. Cr showing significant overlap between Yunling and Viloco cassiterite. B: Compared to Viloco cassiterite, Yunling cassiterite (except the black samples) contains lower tungsten-uranium. C and D: Trace element plots potentially separating cassiterite from the two deposits, based on lower concentrations of iron and antimony in Yunling cassiterite.

CONCLUSIONS

The Yunling area in Yunnan Province, China, is among the few sources of gem cassiterite, producing mineral specimens since the 1980s. Despite the influx of faceted stones on the Chinese market in recent years, a lack of knowledge of their gemological properties and trace element chemistry exists, a gap this article addresses.

A detailed gemological investigation shows various hues of cassiterite, including near-colorless, light brown, brown, brownish pink, red, light gray, and black. Color bands displaying an oscillatory nature and irregular gray-black color domains are common. Notable mineral inclusions are tourmaline, beryl, and mica. Three-phase fluid inclusions, frequently found in healed fissures, consist of liquid, vapor, and a daughter mineral, probably halite.

Quantitative chemical analysis using LA-ICP-MS showed that the trace elements in the seven color groups of Yunling cassiterite are dominated by titanium (avg. 343 ppmw) and iron (avg. 122 ppmw). Additionally, black samples exhibited significant enrichment in tungsten (avg. 183 ppmw) and uranium (avg. 12 ppmw). The UV-Vis-NIR absorption spectra of the various samples exhibited significant differences, illustrating different sources for the various colors. The black color can be attributed to the presence of trace element tungsten and oxygen vacancies, while the brown color may result from the presence of oxygen vacancies alone. The color of the red sample could be attributed to the contribution of iron

oxide staining within fractures, so this color is not inherently from the host crystal. The underlying cause of pink color remains unresolved and requires further investigation.

Yunling cassiterite typically shows a narrower range of trace element concentrations (e.g., titanium, cobalt, nickel, and chromium) than samples from the renowned deposit in Viloco, Bolivia. Trace element plots of Sb-Ni and Fe-Nb can efficiently discriminate Yunling and Viloco cassiterite. The refinement of geographic origin determination for cassiterite, through additional reliable samples and data from this and other sites, remains an area for further study.

ABOUT THE AUTHORS

Dr. Wenqing Huang (corresponding author, 67019822@qq.com), Professor Jungui Zhou, and Shuxin Dong are affiliated with the National Center of Inspection and Testing on Quality of Gold and Silver Products, Nanjing Institute of Product Quality Inspection in Nanjing. Ting Shui is a professor at Nanjing Center, China Geological Survey in Nanjing. Dr. Junyi Pan (as well as Dr. Huang) is affiliated with State Key Laboratory for Mineral Deposits Research, Institute of Geo-Fluids, Frontiers Science Center for Critical Earth Material Cycling, School of Earth Sciences and Engineering, Nanjing University. Professor Fanwei Meng is affiliated with the School of Resources and Geosciences, China University of Mining and Technology in Xuzhou. Rui Zuo and Suqiao Cao are with the Anhui Provincial Institute of Geological Experiments in Hefei.

ACKNOWLEDGMENTS

The authors would like to thank Yongming Shi for providing valuable photos and related information. This work is financially supported by the National Nature Science Foundation of China (grant number 42272094), the Natural Science Foundation of Jiangsu Province (grant number BK20221171), the Open Foundation of State Key Laboratory for Mineral Deposits Research, Nanjing University (grant number 2023-LAMD-K03), and Natural Resources Science and Technology Project of Anhui Province (grant number 2022-K-12). We sincerely thank the anonymous peer reviewers for feedback that substantially improved the quality of this article.

REFERENCES

Bennett J.M. (2021) On the geochemistry of cassiterite. PhD thesis. University of Western Australia, 191 pp.

Bennett J.M., Kemp A.I.S., Roberts M.P. (2020) Microstructural controls on the chemical heterogeneity of cassiterite revealed by cathodoluminescence and elemental X-ray mapping. *American Mineralogist*, Vol. 105, No. 1, pp. 58–76, http://dx.doi.org/10.2138/am-2020-6964

Chen L.L., Ni P., Dai B.Z., Li W.S., Chi Z., Pan J.Y. (2019) The genetic association between quartz vein-and greisen-type mineralization at the Maoping W–Sn deposit, southern Jiangxi, China: Insights from zircon and cassiterite U–Pb ages and cassiterite trace element composition. *Minerals*, Vol. 9, No. 7, article no. 411, http://dx.doi.org/10.3390/min9070411

Chen X.C., Hu R.Z., Bi X.W., Li H.M., Lan J.B., Zhao C.H., Zhu J.J. (2014) Cassiterite LA-MC-ICP-MS U/Pb and muscovite $^{40}Ar/^{39}Ar$ dating of tin deposits in the Tengchong-Lianghe tin district, NW Yunnan, China. *Mineralium Deposita*, Vol. 49, pp. 843–860, http://dx.doi.org/10.1007/s00126-014-0513-8

Cohen A.J., Adekeye J.I.D., Hapke B., Partlow D.P. (1985) Interstitial Sn^{2+} in synthetic and natural cassiterite crystals. *Physics and Chemistry of Minerals*, Vol. 12, No. 6, pp. 363–369, http://dx.doi.org/10.1007/BF00654347

Crowningshield G.R. (1960) Developments and Highlights at the Gem Trade Lab in New York: Unusual stones. *G&G*, Vol. 10, No. 2, pp. 61–62.

Deer W.A., Howie R.A., Zussman J. (1992) *An Introduction to the Rock-Forming Minerals*. Longman Group UK Ltd., Harlow, UK.

Deng J., Wang Q., Li G., Li C., Wang C. (2014) Tethys tectonic evolution and its bearing on the distribution of important mineral deposits in the Sanjiang region, SW China. *Gondwana Research*, Vol. 26, No. 2, pp. 419–437, http://dx.doi.org/10.1016/j.gr.2013.08.002

Farmer C.B., Searl A., Halls C. (1991) Cathodoluminescence and growth of cassiterite in the composite lodes at South Crofty mine, Cornwall, England. *Mineralogical Magazine*, Vol. 55, No. 380, pp. 447–458, http://dx.doi.org/10.1180/minmag.1991.055.380.14

Frezzotti M.L., Tecce F., Casagli A. (2012) Raman spectroscopy for fluid inclusion analysis. *Journal of Geochemical Exploration*, Vol. 112, pp. 1–20, http://dx.doi.org/10.1016/j.gexplo.2011.09.009

Fritsch E., Rossman G.R. (1987) An update on color in gems. Part 1: Introduction and colors caused by dispersed metal ions. *G&G*, Vol. 23, No. 3, pp. 126–139, http://dx.doi.org/10.5741/GEMS.23.3.126

——— (1988a) An update on color in gems. Part 2: Colors involving multiple atoms and color centers. *G&G*, Vol. 24, No. 1, pp. 3–15, http://dx.doi.org/10.5741/GEMS.24.1.3

——— (1988b) An update on color in gems. Part 3: Colors caused by band gaps and physical phenomena. *G&G*, Vol. 24, No. 2, pp. 81–102, http://dx.doi.org/10.5741/GEMS.24.2.81

Gaievskyi I., Iemelianov I. (2012) Gem News International: Black cassiterite. *G&G*, Vol. 48, No. 1, p. 63.

Gemmrich L., Torró L., Melgarejo J.C., Laurent O., Vallance J., Chelle-Michou C., Sempere T.P.A. (2021) Trace element composition and U-Pb ages of cassiterite from the Bolivian tin belt. *Mineralium Deposita*, Vol. 56, No. 8, pp. 1491–1520, http://dx.doi.org/10.1007/s00126-020-01030-3

Goncharov G.N., Filatov S.K. (1971) Typical structural features of cassiterite from Sherlovaya Gora. *Geochemistry International*, Vol. 8, No. 2, pp. 268–275.

Grigor'yev I.F., Dolomanova Y.I., Podol'skiy A.M., Solntseva L.S., Solntsev B.N. (1986) Dependence of the structural type of cassiterite on its origin. *International Geology Review*, Vol. 28, No. 6, pp. 662–669, http://dx.doi.org/10.1080/00206818609466306

Grubb P.L.C., Hannaford P. (1966) Ferromagnetism and colour zoning in some Malayan cassiterite. *Nature*, Vol. 209, No. 5024, pp. 677–678, http://dx.doi.org/10.1038/209677a0

Gu J.S. (2010) Verification report on the reserves of mineral resources in the Yunling tin mine mining area, Yongde County, Yunnan Province. *Yunnan Geological Survey Report*, 127 pp. [in Chinese].

Guillong M., Meier D.L., Allan M.M., Heinrich C.A., Yardley B.W. (2008) Appendix A6: SILLS: A MATLAB-based program for the reduction of laser ablation ICP-MS data of homogeneous materials and inclusions. *Mineralogical Association of Canada Short Course*, Vol. 40, pp. 328–333.

Guo J., Zhang R., Li C., Sun W., Hu Y., Kang D., Wu J. (2018) Genesis of the Gaosong Sn–Cu deposit, Gejiu district, SW China: Constraints from *in situ* LA-ICP-MS cassiterite U–Pb dating and trace element fingerprinting. *Ore Geology Reviews*, Vol. 92, pp. 627–642, http://dx.doi.org/10.1016/j.oregeorev.2017.11.033

Harris J.R., Williamson M.C., Percival J.B., Behnia P., Macleod R.F. (2015) Detecting and mapping gossans using remotely-sensed data. In M.C. Williamson, Ed., *Environmental and Economic Significance of Gossans*. Geological Survey of Canada, Open file 7718, Ottawa, Ontario, Canada, pp. 3–13.

He X., Zhao J., Zhou R., Feng Y., Leonard N., Li F., Liu Z., Li W., Tan S. (2022) The distribution and substitution mechanism of trace elements in cassiterites: Constraints from LA-ICP-MS U-Pb dating, elemental mapping and *in situ* trace element analyses of the Gejiu tin polymetallic deposit, SW China. *Chemical Geology*, Vol. 609, article no. 121063, http://dx.doi.org/10.1016/j.chemgeo.2022.121063

Hennigh Q., Hutchinson R.W. (1999) Cassiterite at Kidd Creek: An example of volcanogenic massive sulfide-hosted tin mineralization. In M.D. Hannington and C.T. Barri, Eds., *The Giant Kidd Creek Volcanogenic Massive Sulfide Deposit, Western Abitibi Subprovince, Canada*. Economic Geology Publishing Co., Inc., Littleton, Colorado, pp. 431–440.

Huang W.Q., Pan J.Y. (2021) Gem Notes: Cassiterite from Yunnan Province, China. *Journal of Gemmology*, Vol. 37, No. 8, pp. 766–767.

Huang W.Q., Ni P., Pan, J.Y., Zhou J.G., Shui T., Chen H., Fan M.S., Cui J.M., Meng F.W., Ding J.Y. (2023) Relationship between cathodoluminescence response and trace element characterization of cassiterite from the Yunling tin deposit in western Yunnan, China: Implications for substitution mechanism and ore genesis. *Ore Geology Reviews*, Vol. 161, article no. 105610, http://dx.doi.org/10.1016/j.oregeorev.2023.105610

Hyršl J. (2002) Gem News International: Cassiterite from Viloco, Bolivia. *G&G*, Vol. 38, No. 2, pp. 175–176.

Hyršl J., Petrov A. (1998) Gemstones and ornamental stones from Bolivia: A review. *Journal of Gemmology*, Vol. 26, No. 1, pp. 41–47.

Ishida S., Hayashi M., Kato I. (1987) Spectroscopic study of chemical state and coloration of chromium in tin oxide. *Journal of the Ceramic Association, Japan*, Vol. 95, No. 3, pp. 303–308, http://dx.doi.org/10.2109/jcersj1950.95.1099_303 [in Japanese with English abstract].

Kojima M., Kato H., Gatto M. (1996) Optical and electrical properties of amorphous Sb-Sn-O thin films. *Philosophical Magazine B*, Vol. 73, No. 2, pp. 277–288, http://dx.doi.org/10.1080/01418639609365824

Lafuente B., Downs R.T., Yang H., Stone N. (2016) The power of databases: The RRUFF project. In T. Armbruster and R.M. Danisi, Eds., *Highlights in Mineralogical Crystallography*, pp. 1–29. W. de Gruyter GmbH, Berlin.

Lehmann B. (2021) Formation of tin ore deposits: A reassessment. *Lithos*, Vol. 402–403, article no. 105756, http://dx.doi.org/10.1016/j.lithos.2020.105756

Lensing-Burgdorf M., Watenphul A., Schlüter J., Mihailova B. (2017) Crystal chemistry of tourmalines from the Erongo Mountains, Namibia, studied by Raman spectroscopy. *European Journal of Mineralogy*, Vol. 29, No. 2, 257–267, http://dx.doi.org/10.1127/ejm/2017/0029-2607

Lopez-Navarrete E., Caballero A., Orera V.M., Lázaro F.J., Ocaña M. (2003) Oxidation state and localization of chromium ions in Cr-doped cassiterite and Cr-doped malayaite. *Acta Materialia*, Vol. 51, No. 8, pp. 2371–2381, http://dx.doi.org/10.1016/S1359-6454(03)00044-2

Li Y.N. (1985) Geological reconnaissance report of tin prospecting in Yunling area, Yongde County, Yunnan Province. *Yunnan Geological Survey Report*, 178 pp. [in Chinese].

Mao W., Zhong H., Yang J., Tang Y., Liu L., Fu Y., Zhang X., Sein K., Myint Aung S., Li J., Zhang L. (2020) Combined zircon, molybdenite, and cassiterite geochronology and cassiterite geochemistry of the Kuntabin tin-tungsten deposit in Myanmar. *Economic Geology*, Vol. 115, No. 3, pp. 603–625, http://dx.doi.org/10.5382/econgeo.4713

Matsushima Y., Maeda K., Suzuki T. (2008) Nature of dark-brown SnO_2 films prepared by a chemical vapor deposition method. *Journal of the Ceramic Society of Japan*, Vol. 116, No. 1357, pp. 989–993, http://dx.doi.org/10.2109/jcersj2.116.989

Möller P., Dulski P., Szacki W., Malow G., Riedel E. (1988) Substitution of tin in cassiterite by tantalum, niobium, tungsten, iron and manganese. *Geochimica et Cosmochimica Acta*, Vol. 52, No. 6, pp. 1497–1503, http://dx.doi.org/10.1016/0016-7037(88)90220-7

Moore T. (2004) What's new in minerals: Tucson Show 2004. *Mineralogical Record*, Vol. 35, No. 3, pp. 249–263.

Murciego A., Sanchez A.G., Dusausoy Y., Pozas J.M.M., Ruck, R. (1997) Geochemistry and EPR of cassiterites from the Iberian Hercynian Massif. *Mineralogical Magazine*, Vol. 61, No. 406, pp. 357–365, http://dx.doi.org/10.1180/minmag.1997.061.406.03

Nambaje C., Eggins S.M., Yaxley G.M., Sajeev K. (2020) Microcharacterisation of cassiterite by geology, texture and zonation: A case study of the Karagwe Ankole Belt, Rwanda. *Ore Geology Reviews*, Vol. 124, article no. 103609, http://dx.doi.org/10.1016/j.oregeorev.2020.103609

Neiva A.M.R. (1996) Geochemistry of cassiterite and its inclusions and exsolution products from tin and tungsten deposits in Portugal. *Canadian Mineralogist*, Vol. 34, No. 4, pp. 745–768.

Ni P., Pan J.Y., Han L., Cui J.M., Gao Y., Fan M.S., Li W.S., Chi Z., Zhang K.H., Cheng Z.L., Liu Y.P. (2023) Tungsten and tin deposits in South China: Temporal and spatial distribution, metallogenic models and prospecting directions. *Ore Geology Reviews*, Vol. 157, article no. 105453, http://dx.doi.org/10.1016/j.oregeorev.2023.105453

Nie F., Dong G.C., Mo X.X., Zhu D.C., Dong M.L., Wang X. (2012) Geochemistry, zircon U-Pb chronology of the Triassic granites in the Changning-Menglian suture zone and their implications. *Acta Petrologica Sinica*, Vol. 28, No. 5, pp. 1465–1476 [in Chinese with English abstract].

Nomiya K., Sugie Y., Amimoto K., Miwa M. (1987) Charge-transfer absorption spectra of some tungsten (VI) and molybdenum (VI) polyoxoanions. *Polyhedron*, Vol. 6, No. 3, pp. 519–524, http://dx.doi.org/10.1016/S0277-5387(00)81018-9

Ollila J.T. (1986) Origin of colour zoning in cassiterites from tin deposits within the Bushveld complex, South Africa. *Bulletin of the Geological Society of Finland*, Vol. 58, No. 2, pp. 3–11, http://dx.doi.org/10.17741/bgsf/58.2.001

Ottens B. (2008) *China: Mineralien - Fundstellen - Lagerstätten*, Christian Weise Verlag, Munich [in German].

——— (2021) *China II: Mineralien - Fundstellen - Lagerstätten*. Christian Weise Verlag, Munich [in German].

Pavlova G.G., Palessky S.V., Borisenko A.S., Vladimirov A.G., Seifert T., Phan L.A. (2015) Indium in cassiterite and ores of tin deposits. *Ore Geology Reviews*, Vol. 66, pp. 99–113, http://dx.doi.org/10.1016/j.oregeorev.2014.10.009

Renfro N. (2015) Digital photomicrography for gemologists. *G&G*, Vol. 51, No. 2, pp. 144–159, http://dx.doi.org/10.5741/GEMS.51.2.144

Serment B., Gaudon M., Toulemonde O., Duttine M., Brochon C., Demourgues A. (2019) Tuning the Cr^{IV}/Cr^{III} valence states in purple Cr-doped SnO_2 nanopowders: The key role of Cr^{IV} centers and defects. *Inorganic Chemistry*, Vol. 59, No. 1, pp. 678–686, http://dx.doi.org/10.1021/acs.inorgchem.9b02943

Shannon R.D. (1976) Revised effective ionic radii and systematic studies of interatomic distances in halides and chalcogenides. *Acta Crystallographica Section A*, Vol. 32, No. 5, pp. 751–767, http://dx.doi.org/10.1107/S0567739476001551

Swart P.K., Moore F. (1982) The occurrence of uranium in association with cassiterite, wolframite, and sulphide mineralization in South-West England. *Mineralogical Magazine*, Vol. 46, No. 339, pp. 211–215, http://dx.doi.org/10.1180/minmag.1982.046.339.07

Tena M.A., Sorlí S., Llusar M., Badenes J.A., Forés A., Monrós G. (2005) Study of Sb-doped SnO_2 gray ceramic pigment with cassiterite structure. *Journal of Inorganic and General Chemistry*, Vol. 631, No. 11, pp. 2188–2191, http://dx.doi.org/10.1002/zaac.200570038

Tindle A.G., Breaks F.W. (1998) Oxide minerals of the Separation Rapids rare-element granitic pegmatite group, northwestern Ontario. *Canadian Mineralogist*, Vol. 36, No. 2, pp. 609–635.

Wang A., Freeman J.J., Jolliff B.L. (2015) Understanding the Raman spectral features of phyllosilicates. *Journal of Raman Spectroscopy*, Vol. 46, No. 10, pp. 829–845, http://dx.doi.org/10.1002/jrs.4680

Wang C.M., Deng J., Carranza E.J.M., Santosh M. (2014) Tin metallogenesis associated with granitoids in the southwestern Sanjiang Tethyan Domain: Nature, deposit types, and tectonic setting. *Gondwana Research*, Vol. 26, No. 2, pp. 576–593, http://dx.doi.org/10.1016/j.gr.2013.05.005

Wu S.Z. (2013) *Gems and Mineral Crystals from Yunnan Province*. Yunnan Technology Publishing House, Kunming, China, 221 pp. [in Chinese].

Wu F., Liu X., Ji W., Wang J., Yang L. (2017) Highly fractionated granites: Recognition and research. *Science China Earth Sciences*, Vol. 60, pp. 1201–1219.

Xiao K., Sun X., Li Q., Si X.B., Zheng X., Lu L.L., Zhao Z.Y. (2022) Geological characteristics and zircon U-Pb geochronology of granite in Yunling tin deposit, southwestern Yunnan. *Mineral Deposits*, Vol. 41, No. 1, pp. 21–34 [in Chinese with English abstract].

Yang L.G., Dong W.W., Tan B.F., Chen S.L., Deng Y., Wang Q.H. (1998) Geological reconnaissance of the tin deposits in the Yunling area, Yalian Country, Yongde County, Yunnan Province. *Yunnan Geological Survey Report*, 39 pp. [in Chinese].

Yu X.H., Xiao X.N., Yang G.L., Mo X.X., Zeng P.S., Wang J.L. (2008) Zircon SHRIMP dating of several granites and geological significance in southern part of "Sanjiang" area, western Yunnan Province. *Acta Petrologica Sinica*, Vol. 24, No. 2, pp. 377–383 [in Chinese with English abstract].

Zhang X.Y., Peng R.M., Li Z.L., Luo P.H., Li J.W., Yi A.W. (2012) Geochemical characteristics of Yunling granodiorite in the Damaidi Sn ore district, southwest Yunnan. *Geophysical & Geochemical Exploration*, Vol. 36, No. 4, pp. 567–572 [in Chinese with English abstract].

Zhou C., Li Y., Chen Y., Lin J. (2018) Hydrothermal synthesis of tungsten doped tin dioxide nanocrystals. *Materials Research Express*, Vol. 5, No. 1, article no. 015911, http://dx.doi.org/10.1088/2053-1591/aaa7a4